Article: Remote sensing of lunar aureole with a sky camera: Adding information in the nocturnal retrieval of aerosol properties with GRASP code

Authors: R. Román, B. Torres, D. Fuertes, V.E. Cachorro, O. Dubovik, C. Toledano, A. Cazorla, A. Barreto, J.L. Bosch, T. Lapyonok, R. González, P. Goloub, M.R. Perrone, F.J. Olmo, A. de Frutos, L. Alados-Arboledas

Remote sensing of lunar aureole with a sky camera: Adding information in the nocturnal retrieval of aerosol properties with GRASP code

R. Román[a,b,c], B. Torres[d,e], D. Fuertes[e], V.E. Cachorro[a], O. Dubovik[d], C. Toledano[a], A. Cazorla[b,c], A. Barreto[f,a,i], J.L. Bosch[b,c,g], T. Lapyonok[d], R. González[a], P. Goloub[d], M.R. Perrone[h], F.J. Olmo[b,c], A. de Frutos[a], L. Alados-Arboledas[b,c]

[a]Atmospheric Optics Group (GOA), University of Valladolid (Spain)

[b]Department of Applied Physics, University of Granada. 18071, Granada (Spain)

[c]Andalusian Institute for Earth System Research (IISTA-CEAMA), University of Granada, Autonomous Government of Andalusia. 18006, Granada (Spain)

[d]Laboratoire d'Optique Atmosphérique, CNRS, Lille 1 University (France)

[e]Generalized Retrieval of Atmosphere and Surface Properties - SAS (France)

[f]Cimel Electronique, Paris, France

[g]Departamento Ingeniería Eléctrica y Térmica, University of Huelva (Spain)

[h]Dipartimento di Matematica e Fisica, Università del Salento, Lecce (Italy)

[i]Izaña Atmospheric Research Center, Meteorological State Agency of Spain, Izaña (Spain)

Correspondence to: R. Román (robertor@goa.uva.es)

Abstract

The use of sky cameras for nocturnal aerosol characterization is discussed in this study. Two sky cameras are configured to take High Dynamic Range (HDR) images at Granada and Valladolid (Spain). Some properties of the cameras, like effective wavelengths, sky coordinates of each pixel and pixel sensitivity, are characterized. After that, normalized camera radiances at lunar almucantar points (up to 20º in azimuth from the Moon) are obtained at three effective wavelengths from the HDR images. These normalized radiances are compared in different case studies to simulations fed with AERONET aerosol information, giving satisfactory results. The obtained uncertainty of normalized camera radiances is around 10% at 533 nm and 608 nm and 14% for 469 nm. Normalized camera radiances and six spectral aerosol optical depth values (obtained from lunar photometry) are used as input in GRASP code (Generalized Retrieval of Aerosol and Surface Properties) to retrieve aerosol properties for a dust episode over Valladolid. The retrieved aerosol properties (refractive indices, fraction of spherical particles and size distribution parameters) are in agreement with the nearest diurnal AERONET products. The calculated GRASP retrieval at night time shows an increase in coarse mode concentration along the night, while fine mode properties remained constant.

Keywords

Sky camera, Moon, GRASP, Aerosol, High Dynamic Range.

1.-Introduction

Aerosols have an important impact on the weather and climatic system and their contribution to the total radiative forcing estimation remains as the most uncertain [IPCC, 2014]. Depending on their properties, aerosols can increase the cooling or warming of the Earth surface by two mechanisms [Haywood and Boucher, 2000; Lohmann and Feichter, 2005]: the direct extinction (scattering and absorption) of solar and thermal radiation (direct effect), and acting as cloud droplet nuclei that leads to changes in the cloud properties and lifetime (indirect effect).

At night there is no solar radiation, but aerosol radiative forcing in the longwave range can be significant for large particles like desert dust and sea salt [Stier et al., 2007; Sicard et al., 2014]. In addition, at night the aerosol indirect effect still works and could provide changes on nocturnal cloud properties [Ramanathan et al., 2001; Kaufman et al. 2005; Rosenfeld et al. 2006]. These changes could contribute to global warming since clouds at night absorb part of the longwave radiation emitted by Earth, and then, they re-emit radiation back to the Earth surface [Ramanathan et al., 1989; NASA Facts, 1999; Wild, 2012]. Moreover, the knowledge of aerosol properties at night is important for the aerosol characterization in polar areas and in winter seasons, which present low sunshine duration values [Stone et al., 2010; Tomasi et al., 2015].

Some instruments and techniques are used for the characterization of aerosol properties at night: lidar systems provide backscatter and extinction profiles using Klett-Fernald-Sasano retrievals [Klett, 1981, 1985; Fernald, 1984; Sasano, 1984] and Raman measurements [Ansmann et al., 1990]; in-situ equipment can provide an accurate aerosol characterization but only for the local point where it is installed and not for the whole atmospheric column [McMurry et al., 2000; Rodríguez et al., 2012]; star and lunar

photometry provides aerosol optical depth (AOD) at different wavelengths [Ansmann et al., 2001; Pérez-Ramírez et al., 2008, 2011; Berkoff et al., 2011; Barreto et al., 2013, 2016, 2017]. The AOD measurements at night provide information to discriminate between the extinction of fine and coarse mode [O'Neill et al., 2003]. They are also useful for obtaining a reliable characterization of the fine mode properties, though the characterization of the coarse mode is less accurate [Torres et al., 2016].

Spectral AOD together with sky radiance provides adequate information to retrieve aerosol microphysical/optical properties (absorption and scattering) during daytime [Dubovik and King, 2000]. That is the case of the AERONET network (AErosol RObotic NETwork; http://aeronet.gsfc.nasa.gov), which provides these diurnal properties from sun/sky photometers distributed around the world [Holben et al., 1998]. At night, the sky radiances near the Moon (lunar aureole) could be used as a source of aerosol scattering information, at least between quarters when the Moon is brighter. This information could be combined with the spectral AOD, also obtained from the Moon (lunar photometry) to retrieve aerosol characteristics.

A sky camera can be used to obtain relative sky radiance near the Moon since it records the full hemispherical sky radiance measuring different wavelength intervals and it can operate at night with an appropriate exposure time (ET). It should be noted also that sky cameras usually present a low signal to noise ratio. Cloud detection is the most spread use of sky cameras [Long et al., 2006; Calbó and Sabburg, 2008; Cazorla et al., 2008a; Ghonima et al., 2012; Kazantzidis et al., 2012; Mandat et al., 2014, Alonso et al., 2014] though they have been used with other purposes [Horváth et al., 2002; Cazorla et al., 2008b; Kreuter et al., 2009; Sigernes et al., 2014], including the retrieval of sky radiances in daytime [Voss and Zibordi, 1989; López-Alvarez et al., 2008; Román et al., 2012; Toshing et al., 2013; Chauvin et al., 2015].

126   The main goal of this work is to propose and validate the use of sky cameras to

127   obtain normalized radiances in the lunar aureole region. The secondary goal consists of

128   using those normalized radiances as inputs in an inversion algorithm together with

129   spectral AOD measurements (gained by lunar photometry) to retrieve aerosol properties

130   during night time.

131   This paper is structured as follows: Section 2 presents the sites and

132   instrumentation used in this work. The characterization of the sky camera and the

133   methodology used to obtain normalized radiances are explained in Section 3. Section 4

134   introduces the GRASP code. A thorough comparison between normalized camera

135   radiances and simulations is developed in Section 5. The GRASP inversion of camera

136   radiances and AOD for a particular case is also shown in Section 5. Finally, Section 6

137   summarizes the main conclusions.

138

139   2 -Location and ancillary instrumentation

140   The present work utilizes data from Granada and Valladolid (both located in

141   Spain). Valladolid is an urban area, surrounded by rural areas, sited in North-Central

142   Iberian Peninsula (150 km North from Madrid) with a population of ~300.000 inhabitants.

143   Román et al. [2014b] characterized the predominant aerosol at Valladolid as "continental

144   clean" obtaining monthly mean values of the AOD at 443 nm ranging from 0.10 to 0.24,

145   and Angström Exponent (AE) from 0.9 to 1.5, showing higher/lower AOD/AE values in

146   summer due to episodic Saharan dust events [Cachorro et al., 2016]. Granada, located in

147   the South-East of the Iberian Peninsula, is a medium-sized and non-industrialized city

148   situated in a natural basin surrounded by mountains and with a population similar to

149   Valladolid; the local aerosol sources are mainly the heavy traffic (particularly diesel

150 vehicles) together with the re-suspension of material available on the ground, especially

151 during the warm season. In winter, domestic heating (based on fuel oil combustion) also

152 represents an important anthropogenic aerosol source [Lyamani et al., 2010; 2011; Titos

153 et al., 2012; 2014]. AERONET provides a climatology table (Level 2.0) for Granada with

154 monthly mean values of the AOD at 500 nm between 0.10 and 0.20 and AE values

155 between 0.8 to 1.4, being AOD/AE values higher/lower in summer, also because of

156 frequent Saharan dust outbreaks.

157 Both places are equipped with a "CHM-15k Nimbus" ceilometer (*Lufft*

158 manufacturer), a "CE318-T" photometer (*Cimel Electronique*) and a "SONA" sky camera

159 (*Sieltec Canarias S.L.*). One "CE318-N" photometer (*Cimel Electronique*) is also

160 installed at Valladolid. These instruments are on the rooftop of the Science faculty of the

161 University of Valladolid (41.66ºN; -4.71ºW; 705 m a.s.l.) and on the rooftop of the

162 Andalusian Institute for Earth System Research (IISTA-CEAMA; 37.16ºN; -3.61ºW; 680

163 m a.s.l.). The mentioned ceilometers belong to the Iberian Ceilometer Network, ICENET,

164 which processes raw data and provides information about the vertical attenuated

165 backscatter at 1064 nm [Cazorla et al., 2017]. This information helps to detect possible

166 changes in the aerosol properties at night.

167 The CE318-N photometer takes measurements of Sun irradiance and sky radiance,

168 and CE318-T photometer also measures lunar direct irradiance, performing daytime and

169 night time photometric measurements [Barreto et al., 2016]. The photometer #914

170 (CE318-T) was available for a short campaign at Valladolid and used in this work. For

171 the rest of the period, the photometer #788 or the photometer #383 (both CE318-N),

172 located at the same station, were used. Both photometers belong to the RIMA network

173 (Iberian network for aerosol measurements), which is federated to AERONET. The #918

174 (CE318-T), used for this work at Granada, belongs to I-AMICA (Infrastruttura di Alta

175   Tecnologia per il Monitoraggio Integrato Climatico-Ambientale of Italy) and operates

176   within AERONET. These instruments are periodically calibrated, following the

177   AERONET protocol, ensuring high quality data. In addition, AERONET processes the

178   photometer data providing a wide set of products such as daytime AOD at 8 wavelengths,

179   aerosol size distribution, fraction of spherical particles (sphere fraction) and refractive

180   indices [Holben et al., 1998; Dubovik et al., 2000, 2006]. Regarding night time

181   measurements, AOD is obtained at 6 wavelengths (440, 500, 675, 870, 1020 and 1640

182   nm) following the method described in Barreto et al. [2016] which uses the ROLO

183   (RObotic Lunar Observatory) model [Kieffer and Stone, 2005] for the lunar

184   extraterrestrial irradiance calculation. ROLO is an empirically-based model that provides,

185   for a given place and time, the spectral extraterrestrial lunar irradiance using the following

186   geometrical variables: lunar phase angle; selenographic latitude and longitude of the

187   observer; and selenographic longitude of the Sun. The calibration of the instrument for

188   lunar measurements was done by the "Lunar Langley Method" explained by Barrreto et

189   al. [2013].

190

191   **3- Sky camera**

192   SONA ("Sistema de Observación de Nubosidad Automático": Automatic Cloud

193   Observation System) sky camera is a device which provides full sky images at day and

194   night. The system was mainly designed for cloud cover detection, but it can be used with

195   other purposes. It is composed of a surveillance CCD camera with a fisheye lens inside a

196   waterproof case and a dome with a shadow band blocking the Sun [González et al., 2012].

197   The CCD sensor provides RGB images with 8 bit-digitalization yielding 256 counts per

198   channel [Cazorla et al., 2015]. The CCD resolution is 640x480 pixels, but the system at

199 Granada site was configured to record images of 480x480 pixels. An infrared (IR) cut-off

200 filter is installed between the CCD and the fisheye lens in a mobile platform in order to

201 block or to allow IR light into the sensor. Both cameras used in this paper were configured

202 to take all images with the IR cut-off filter. The temperature (T) of the CCD is also logged

203 with a resolution of 0.5ºC.

204 **3.1- Camera characterization**

205 **3.1.1- Effective wavelengths**

206 The CCD spectral response, given by the manufacturer, is shown in Fig. 1a. This

207 response is only available up to 700 nm, but red channel seems to have certain sensitivity

208 to longer wavelengths. As mentioned above, the camera also contains an IR cut-off filter

209 to block the longest wavelengths. The spectral response of this filter, given by the

210 manufacturer, is also shown in Fig. 1b. The filter transmittance can be considered constant

211 and with a value about 90% from 400 nm up to 600 nm. At longer wavelengths, the

212 transmittance starts to decrease, being ~50% at 640 nm and below 10% at 700 nm. The

213 total spectral response of the sky camera is the CCD response weighted by the IR cut-off

214 filter transmittance, shown at Fig. 1c. This total spectral response shows that the camera

215 is not sensitive to infrared light above 700 nm, due to the effect of the IR cut-off filter,

216 and presents its highest response in the green channel.

217 Sky radiance is measured in three broadband channels (Fig. 1c) but, as a first

218 approximation, the radiance at these broadband channels can be considered proportional

219 to the radiance at an effective wavelength. This is due to the following fact: the ratio of

220 two broadband measurements, which are taken under different conditions but with the

221 same instrument (the same spectral response), is equal to the ratio of the same

222 measurements taken with an instrument which is only sensitive at the effective

223 wavelength, λ_e, calculated as [Kholopov, 1975; Román et al., 2012]:

224
$$\lambda_e = \frac{\int_\lambda \lambda I(\lambda)S(\lambda)d\lambda}{\int_\lambda I(\lambda)S(\lambda)d\lambda} \tag{1}$$

225 where I is the incoming irradiance to the instrument at the wavelength λ, and S the spectral

226 response of the instrument channel. In order to obtain the effective wavelength of the

227 SONA sky camera channels in this work, the effective wavelength of each channel has

228 been calculated for a half Moon cycle at every midnight from first to third lunar quarter

229 with I calculated using the ROLO model. The average (± standard deviation) of the

230 calculated effective wavelengths is 468.8±0.3 nm, 533.3±0.3 nm and 607.7±0.2 nm for

231 blue, green and red channels, respectively. Finally, these effective wavelengths have been

232 rounded to 469 nm, 533 nm and 608 nm, which approximately is within the standard

233 deviation interval. Román et al. [2012] calculated the effective wavelengths for another

234 sky camera under various aerosol conditions, finding standard deviations around 2 nm,

235 which indicated that effective wavelengths of this kind of sky cameras do not vary largely

236 with the real changes on the incoming radiation.
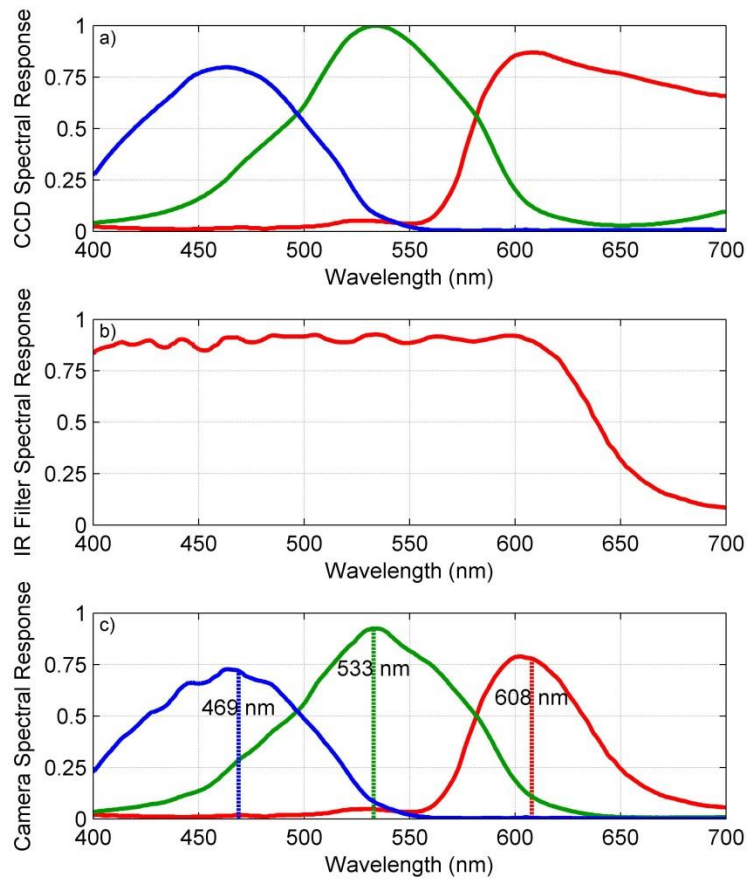
Figure 1: Spectral responses of the three channels (blue, green and red) of the CCD (panel a), of the infrared (IR) cut-off filter (panel b), and of the three channels of the camera (CCD plus infrared cut-off filter; panel c). The effective wavelengths of the camera for lunar applications are marked in panel c.

3.1.2- Sky coordinates of each pixel

SONA sky camera position is fixed, thus every pixel measures the same region of the celestial vault. Hence, the zenith and azimuth angles corresponding to all the pixels can be calculated to locate any celestial body in every image (in this work we focus on the position of the Moon and its aureole). The zenith and azimuth matrices have been calculated using a dataset of sky images under cloud-free conditions and visible stars and planets whose celestial coordinates are well-known in these images. The stellar bodies used at Granada have been Arcturus, Jupiter and Vega; while for Valladolid they have been Altair, Arcturus, Jupiter, Saturn, Vega and Venus. The pixel positions of these stellar bodies have been correlated with their sky coordinates, finding a relationship between the zenith and azimuth with pixel position. As a result, Fig. 2 presents zenith and azimuth

252 calculated for the cameras at Granada (panels a, c and e) and Valladolid (panels b, d and

253 f). The representation of zenith and azimuth angles is similar for both cameras. In both

254 cases, a slight shift in the azimuth can be observed in the north direction. Moreover, the

255 field of view (FOV) of each pixel has been calculated as the solid angle obtained from

256 zenith and azimuth. FOV increases with zenith as can be observed in Fig. 2e and 2f.

257 Figure 2 also shows that Valladolid images have a resolution of 640x480 pixels whereas

258 resolution is 480x480 pixels for Granada. Zenith angles above 80º have been masked in

259 this work since city skylines usually occupy that region.
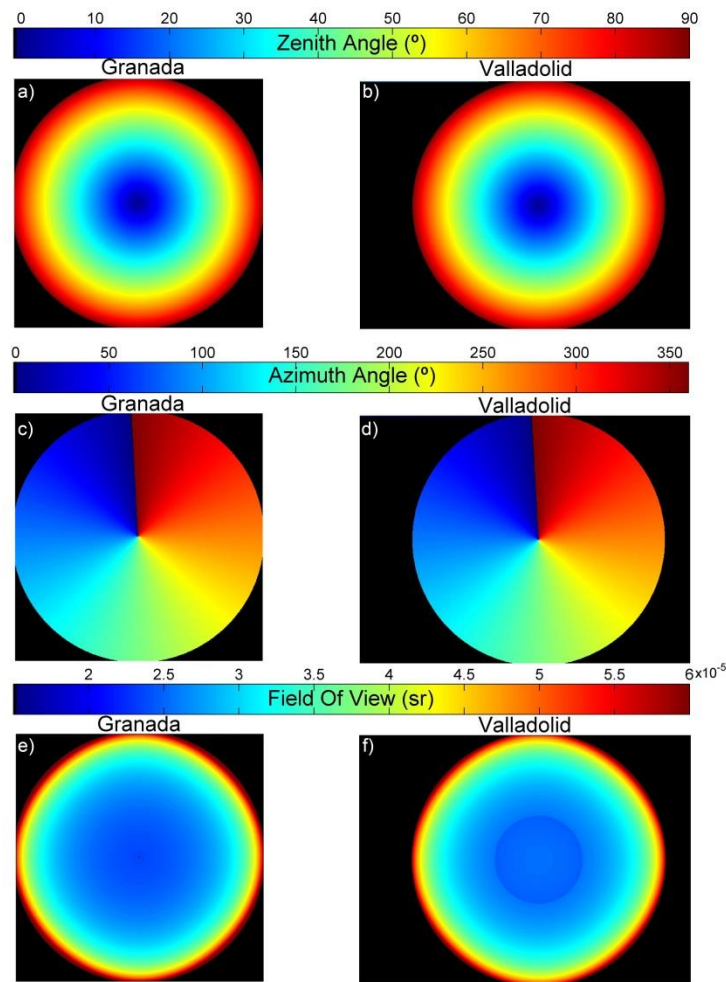

260

261　　　　Figure 2: Zenith (panels a and b), Azimuth (panels c and d) and FOV (panels e and f) viewed by each
262　　camera pixel at Granada (panels a, c and e) and Valladolid (panels b, d and f). Azimuth is defined from 0º
263　　　　　　　　　　　　　(North) to 360º being East 90º and West 270º.

264 **3.1.3- Pixel sensitivity**

12

265   Pixel sensitivity is usually not linear with exposure time in commercial cameras.

266   This is the case for the SONA sky camera. In order to obtain the pixel sensitivity of both

267   cameras, consecutive cloud-free images were taken at different exposure times. Looking

268   at some points of the cloud-free sky, and assuming that the irradiation reaching each pixel

269   must be proportional to the exposure time, the pixel sensitivity function can be obtained

270   by the method explained by Debevec and Malik [1997]. This method uses differently

271   exposed images of the same scene to recover the response function of the imaging

272   process, up to factor of scale, using the assumption of reciprocity. Following this method,

273   the pixel sensitivity of each camera has been calculated under daytime and cloudless

274   conditions for 70 cases distributed in 7 days. These sensitivity values have been averaged

275   for each location, and these averages and their standard deviations are shown in Fig. 3 for

276   both sites and for the three broadband channels. The pixel sensitivity is similar but not

277   equal in the two analyzed cameras. The sensitivity function present similar graphs to those

278   obtained by Debevek and Malik [1997] (see Figs. 2, 4 and 7 of the mentioned paper). The

279   blue channel has the highest sensitivity for low pixel counts, and the saturation effect can

280   be seen at higher pixel counts, where the pixel sensitivity strongly increases. Standard

281   deviation is higher for low pixel counts, which could be associated to fluctuations in the

282   very short exposure times used to reach these pixel counts.
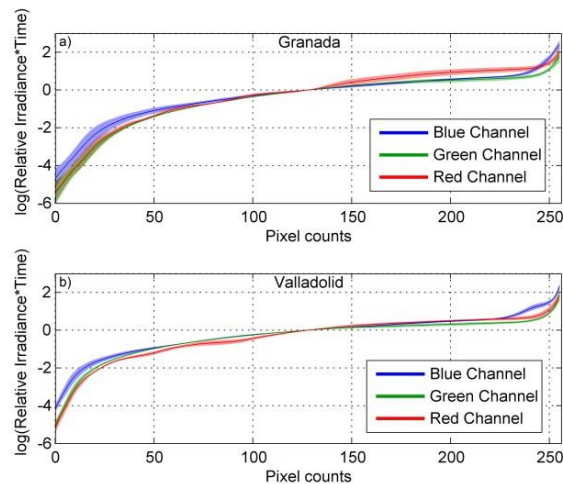
283

Figure 3: Sensitivity of the camera pixels for each channel as a function of pixel counts for both Granada (panel a) and Valladolid (panel b) cameras. The shadow band around the lines represents the standard deviation.

3.1.4- Dark signal

The signal of CCD is not only produced by incoming radiation (photons), but also by thermal energy [Mullikin et al., 1994]; it means that an image taken under dark conditions will show a response different to null, which is called dark image. The response of a dark image usually increases with temperature and with exposure time [Pérez-Ramírez et al., 2008]. These dark images, or dark frames, must be subtracted from an original sky image to remove the thermal noise. Dark signal has been obtained in a different way for both analyzed cameras as detailed below.

The Granada camera was temporally installed in a dark place and covered by an opaque cloth in order to take images in complete dark conditions. Under these dark conditions, the camera recorded dark images at different exposure times and temperature values. The chosen exposure times were the same as the ones that will be shown in Section 3.2.1. The obtained dark images with the same exposure time and temperature have been averaged to reduce the random noise present in single measurements [Urquhart et al., 2015]. These averages have been considered as dark frames (DF). Figure 4 shows the obtained DF (Granada camera) for two different exposure times and three different temperatures. The signal of the frames is shown upscaled by a factor 4 for better visualization. The dark signal is not equal for all pixels under the same conditions of exposure time and temperature. Temperature has a direct effect on DF with a larger dark signal for higher temperatures. An increase in exposure time also produces higher dark signal values.
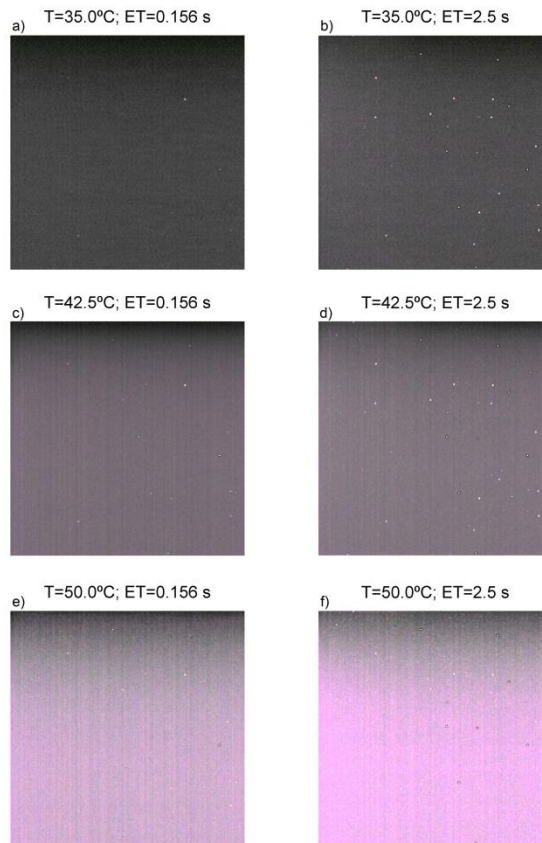
Figure 4: Dark frames obtained with the Granada camera for different temperatures (T) and exposure times (ET). The signal shown is multiplied by 4 in order to be better appreciated.

Figure 5 points out to the same conclusion showing the mode (most frequent value) of all pixels of every dark frame for the channels blue (DF_B), green (DF_G) and red (DF_R) as a function of exposure time and temperature. For low exposure times the dependence of the dark signal on temperature is low but this dark signal presents values higher than zero, indicating the presence of a bias. Dark signal is low while exposure time is below 7 ms, but for higher exposure times it increases especially for high temperatures. For a given exposure time, the dependence of dark signal on temperature presents an exponential behavior. The logarithm of the dark signal (not shown) presents a negative linear relationship with the inverse of the temperature following the Arrhenius law as previously was observed in a different camera by Widenhorn et al. [2002]. The green channel presents the lower dark signals for high temperatures, while red and blue channels

can reach dark signal above 60 digital counts for temperatures near 50ºC and high
exposure times.
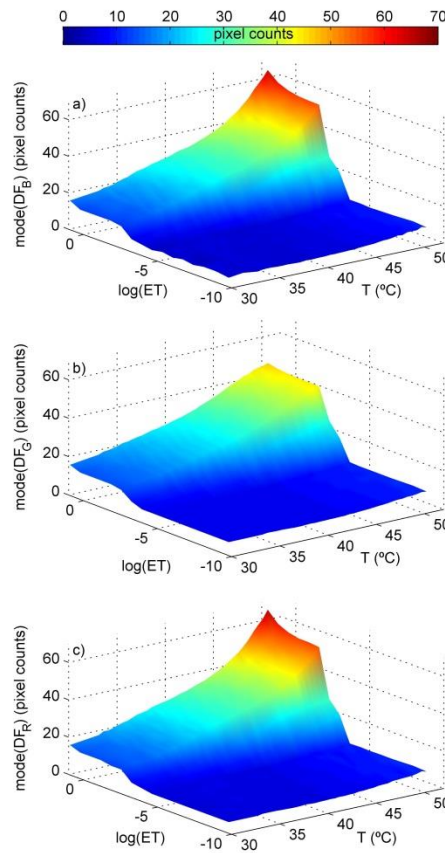
Figure 5: Most frequent value in a dark frame as a function of temperature (T) and logarithm of the
exposure time (ET), for the three Granada camera channels.

The dark frame has been corrected for an original sky image and a given exposure
time and temperature subtracting the DF (obtained for the same exposure time and
temperature) from the non-saturated pixels of the original image. This method has been
applied in this work to the Granada camera, but not to the images recorded by the
Valladolid camera since obtaining the dark frames in a dark place was not feasible. In
order to obtain a dark frame for the Valladolid images, as a first approach, the dark signal
of each channel has been considered the same for all pixels and equal to the average of
the signal of various pixels located in a non-illuminated zone, as in Román et al. [2012].
For Valladolid camera the non-illuminated zone has been considered the 33x24 pixel

rectangle (proportional to the image size) located at the down-right corner of each image. For each channel (R, G and B) the average of the pixel signals in this zone provides a dark signal, and the dark frame (DF_R, DF_G and DF_B) is an image in which all pixels have this same dark signal. Then, for each image taken at Valladolid the calculated DF has been subtracted for the non-saturated pixels.

3.1.5- Hot pixels

Pixels with a very high dark signal are referred as dark current spikes or hot pixels [Widenhorn et al. 2002]. They are generally randomly distributed in a CCD and show up as white, but evenly colored, dots in a dark frame. Hot pixels of the Granada camera can be perfectly appreciated in Fig. 4. The hot pixels of each camera have been determined taking a high exposure image under dark conditions (and low temperature) and considering as hot pixels all the pixels with a signal above 30 digital counts for at least one channel. The obtained hot pixels (not shown) fit well with the hot pixels that can be visually detected in all dark images. Once hot pixels have been identified, they and their neighbors have been masked from all the images.

3.2- Retrieval of relative sky radiance

3.2.1- High Dynamic Range imagery

The CCD provides 256 digital counts per channel, which presents two main problems: some pixels are saturated (in the lunar region in this work), and some pixels are fully dark; pixels in both situations do not provide useful information about the real radiance. The multi-exposure technique has been used to solve both issues [Debevec and Malik, 1997]. It consists of recording the same image at different exposure times, in order to increase the dynamic range, having images where the brightest parts are not saturated (for the lowest exposure times) and images where the darkest parts are bright enough.

361 Once the images at different exposure times are recorded, a linear High Dynamic Range

362 (HDR) image can be obtained using the pixel sensitivity of the camera (to linearize the

363 output) and applying the method of Debevec and Malik [1997]. As a result, a linear HDR

364 image gives, for each channel and pixel, a signal proportional to the incoming irradiance

365 to the CCD [Stumpfel et al., 2014].

366   In this work, the sky cameras have been configured to record 16 consecutive sky

367 images with exposure times following a doubling sequence. The first image (im_1) is taken

368 with an exposure time, $ET(im_1)$, then the second image (im_2) is taken with an exposure

369 time, $ET(im_2)$, equal to $2*ET(im_1)$, then the third (im_3) with an exposure time equal to

370 $2*ET(im_2)=2^2*ET(im_1)$ …, and finally the last image (im_{16}) is taken with a exposure time,

371 $ET(im_{16})=2^{15}*ET(im_1)$, around 2.5 seconds. The elapsed time obtaining the 16-image

372 dataset is about 30 seconds. The gain (ISO) used for these images has been set to constant

373 at at night time, and equal to the one used for obtaining the dark frames (Section 3.1.4).

374 These sequences of 16 images have been taken every five minutes at Granada and

375 Valladolid. As a result, every 5 minutes a linear HDR image has been composed from

376 these 16 images (dark frame corrected) combined with the pixel sensitivity of Fig. 3.

377   For visualization purposes, a linear tone mapped HDR image would show little

378 detail. To improve visualization, the linear HDR images have been tone mapped

379 following the method described by Reinhard et al. [2002]. This method computes the key

380 of the HDR image, a measure of the average logarithmic luminance, and then the image

381 is scaled to the desired brightness level. Figure 6 shows three non-HDR images (panels

382 a, b and c) and the corresponding tone mapped images (panels d, e and f). In the non-

383 HDR images the pixels around the Moon are saturated, especially at Granada, while the

384 signal around the Moon can be discerned in the tone mapped images. Also, the masks

385 covering hot pixels can be appreciated in the HDR images.

386
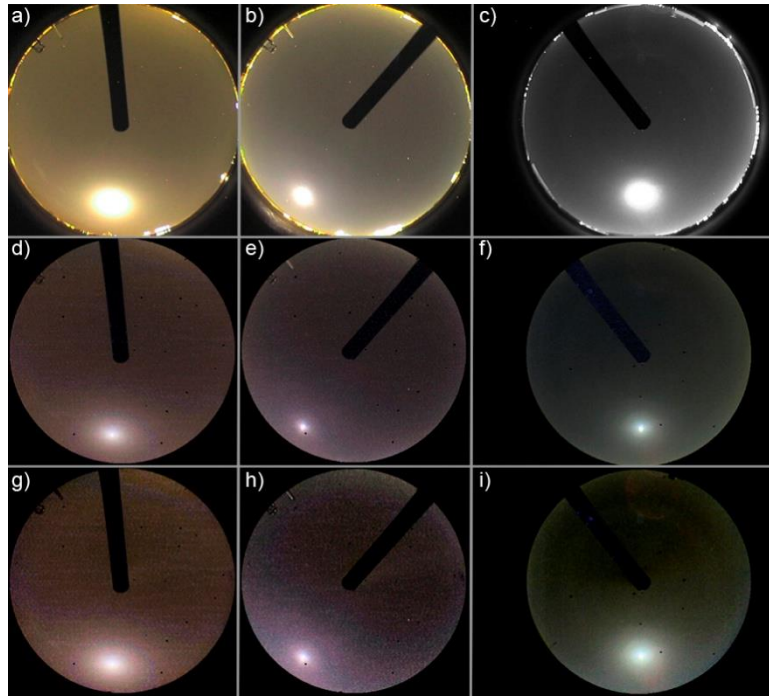
Figure 6: Non-HDR (upper; panels a, b and c) tone mapped sky images before removing background signal (middle; panels d, e and f) and tone mapped sky images with background corrected (bottom; panels g, h and i). Images corresponds to Granada 21st July 2016, 00:40UTC (left; panels a, d and g); Granada 20th May 2015, 21:25UTC (middle; panels b, e and h); Valladolid 3rd August 2015, 02:40UTC (right; panels c, f and i). The non-HDR image at Valladolid was taken under colorless conditions. Pixels with zenith angle above 80º are masked except for non-HDR images.

3.2.2- Point spread function

The point spread function (PSF) is the bidimensional signal viewed by a pixel and its neighbors when this pixel is illuminated by a point source. PSF could cause changes on the variation of the signal between pixels near to an illuminated point source (like the Moon). In this work, PSF has been calculated for both cameras using the method explained by Pinilla et al. (1999) which is based on McGillen et al. (1983) and on Forster and Best (1994). This method basically consists of studying the changes in pixel signal with respect to pixel distance from dark to bright pixels. The first derivative (slope) of the curve of the transition from dark pixels to bright pixels is assumed proportional to the PSF in the selected direction. To this end, diurnal HDR images have been used considering as dark region the pixels containing the camera shadow band, and the bright pixels those containing the blue sky near to the shadow band. For each camera, PSF has

been obtained for 6 different images and then averaged. This PSF has been used to correct the HDR images by a deconvolution of PSF on the image using Lucy-Richardson algorithm (Richardson, 1972; Lucy 1974). This correction helps deblurring some parts of the HDR image. However, the night time images show a larger noise, especially near the Moon, which could be associated to a non-perfect PSF characterization. These results suggest that PSF correction could add noise to the HDR images and, therefore, PSF has not been corrected in this work.

3.2.3- Background correction

The nocturnal sky images also recorded part of the city background light (city lamps, buildings and others). As a consequence, the sky is not fully dark even without Moon. The lunar aureole viewed by the camera can be contaminated by these lights, hence, in order to detect the Moon aureole, the city lights need to be characterized and removed for the original HDR image. With this aim, a data base of background images (BG) has been constructed from images taken under cloud-free conditions and with both Moon Zenith Angle (MZA) and Solar Zenith Angle (SZA) above 100º. In these conditions, we guarantee that the images are not contaminated by the Moon nor the Sun light and neither the clouds. Note that these BG images have been taken at low illumination and they usually are quite noisy. To partially correct for this effect, all the BG images have been smoothed by an averaging filter of 5x5 pixels.

As a first guess, we could assume that the signal of background images depends on the aerosol load, since aerosols can scatter part of the city lights back to the camera. The data base of BG images has been analyzed and correlated to the closest AOD value measurement (note that there are no simultaneous measurements of AOD since BG images are taken under skies without the Sun and Moon). The maximum gap allowed

429   between BG images and AOD measurements has been 3 hours for Granada and 4 hours

430   for Valladolid due to the lower number of images available in the latter. AODs at 440,

431   500 and 675 nm have been assigned to the blue, green and red channels of the camera,

432   respectively. The determination coefficient (r^2) between the pixel signal of each channel

433   and its AOD value has been calculated using the chosen BG images for both cameras

434   (151 images for Granada and 61 for Valladolid). Figure 7 shows the obtained

435   determination coefficient for every pixel, channel and camera, pointing out that red

436   channel presents the best correlation between the background signal and the AOD.

437   However, the correlation is not high, since the r^2 values at Granada are usually below than

438   0.5, 0.4 and 0.2 for the red, green and blue channels, respectively. The correlation at

439   Valladolid is lower, being r^2 below 0.4 in most of pixels for all channels, but this behavior

440   could be explained by the short AOD range used for the calculation of r^2: AOD at 440 nm

441   ranges from 0.03 to 0.13 and AOD at 675 nm from 0.01 to 0.06. However, for Granada

442   camera the AOD intervals have been larger, ranging from 0.03 to 0.35 (AOD at 440 nm)

443   and from 0.01 to 0.33 (AOD at 675 nm). These results indicate that background light does

444   not present a clear dependence on AOD and, therefore, BG images have been considered

445   as independent on aerosol load.
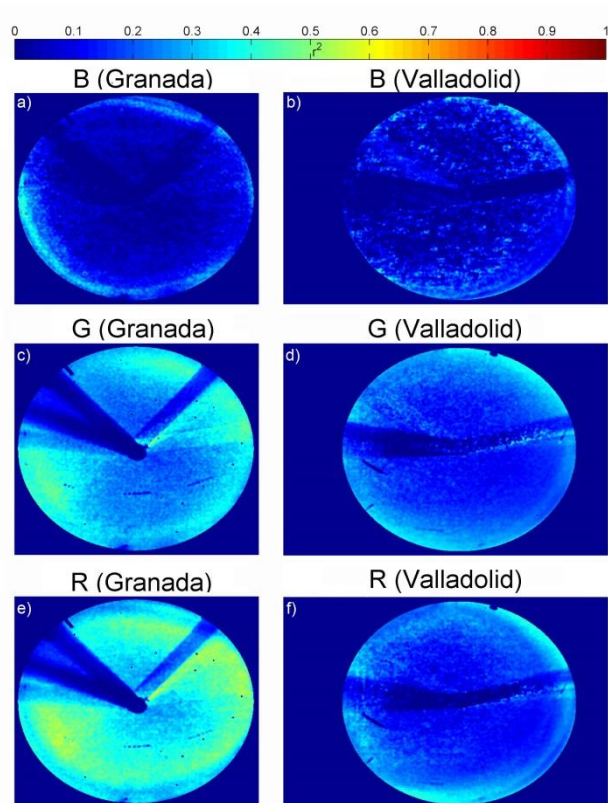
Figure 7: Determination coefficient (r^2) between the background pixel signal and the AOD assumed at each channel. These values are shown for each channel at Granada (left; a-c-e) and Valladolid (right; b-d-f). Pixels with zenith angle above 80º are masked.

Assuming that the background light from the city is constant, an averaged BG image (ABG) has been calculated for each location in order to remove the noise and fluctuations of single BG images. To this end, a set of BG images under clean (low aerosol load) conditions have been chosen, trying to obtain similar conditions for all images despite of the observed low correlation between BG and AOD. The selected night BG images also satisfy that previous and next diurnal AOD at 440 nm measurements were below 0.1. A total of 182 and 156 BG images for Granada and Valladolid, respectively, have been chosen by these criteria, and then they have been averaged. As a result, the ABG has been obtained and is shown in Fig. 8 for Granada and Valladolid, being representative of the background light of each location. ABG images of Fig. 8 include a spot in the sky zenith which is not representative of the background light but it is caused

22

462 by the shadow band, which always block this position. This artefact does not affect results

463 in this work since the Moon never reaches that position.
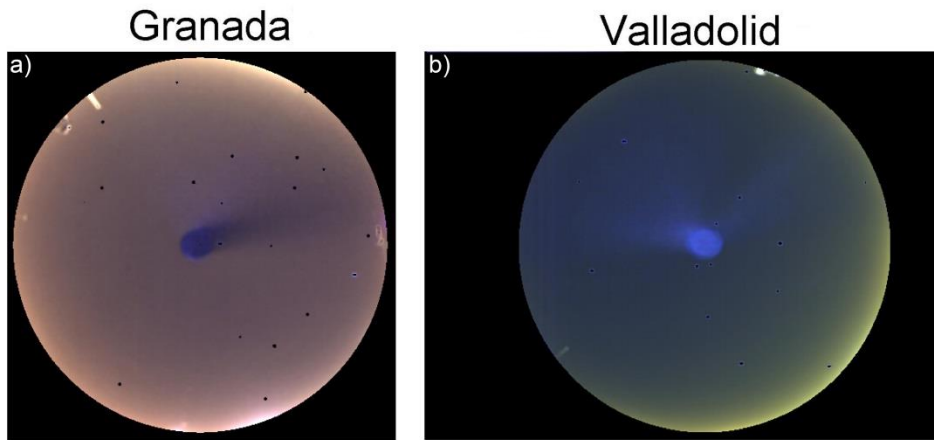
467 Finally, all obtained HDR images have been corrected subtracting the

468 corresponding ABG of Fig. 8. Figures 6g, 6h and 6i present the tone maps of three HDR

469 images after the background correction, showing significant differences against the non-

470 corrected images.

471 **3.2.4- Normalized Lunar Almucantar extraction**

472 Once the background light is removed from the HDR image, the relative radiance

473 at the lunar aureole can be obtained. First, every pixel signal has been divided by its FOV,

474 in order to transform the recorded relative irradiance in the CCD to relative sky radiance

475 (RSR). Several points of the lunar almucantar (points with same zenith angle of the Moon

476 but different azimuths) have been selected and located in the image, and the signal in the

477 pixels within ±0.5º azimuth and ±0.5º zenith have been averaged for each channel. The

478 points selected range from azimuth 3º to 20º azimuth (1º steps) away from the Moon. The

479 first azimuth angle has been chosen at 3º in agreement with the first angle of the

480 almucantar measurements sequence used in the AERONET photometers [Holben et al.,

481 2006]; the last azimuth of 20º has been manually selected since it was observed that

482 beyond 20º the camera signal does not significantly change. In addition, pixel signals

483 which are below the double of the corresponding ABG signal have been discarded even

484 if the azimuth is below 20º. This criterion has excluded several RSR values for very low

485 AOD or low Moon irradiance (at least between the third and first Moon quarters); in both

486 cases the scattered light in the lunar aureole region is low.

487   Once the points of almucantar are selected (3º to 20º and -3º to -20º with at least

488 the double of background signal), both branches of the almucantar have been averaged

489 assuming the sky radiance is symmetric. The number of averaged pixels for each

490 almucantar point (considering its azimuth and its symmetric azimuth) depends on zenith

491 angle because of the lens distortion (see Fig. 2); this number is around 8 pixels for zenith

492 equal to 20º, increasing up to 16 pixels for zenith values of 60º and going down to about

493 12 pixels for zenith equal to 80º. Finally, for each channel, the obtained signals have been

494 normalized by the sum of all of them, giving as result the normalized camera radiance

495 (NCR); the sum of the normalized camera radiances must be 1 for each channel. Then,

496 the normalized camera radiance at a given λ-wavelength and a φ_i-angle has been

497 calculated as:

498
$$NCR_{\lambda,\varphi_i} = \frac{RSR_{\lambda,\varphi_i}}{\sum_{j=1}^{N} RSR_{\lambda,\varphi_j}} \qquad (2)$$

499   where N is the number of points used to extract the almucantar.

500   Figure 9a shows the normalized lunar almucantar radiance obtained using this

501 method for the HDR image on Fig. 6g; the straight lines are the averaged values from

502 both branches, and the azimuth value of the Moon is considered to be 180º.

503

504 4- GRASP code

505   GRASP (Generalized Retrieval of Aerosol and Surface Properties) is a highly

506 accurate algorithm for the retrieval of optical and microphysical aerosol properties and

507 optical surface properties [Dubovik et al., 2014]. GRASP stands out by its versatility (it

508 can be run with a large variety of input variables) and its flexibility (it has the capacity to

509 incorporate and exchange different methods, modules and libraries). This code has been

510 used by other authors with lidar systems, photometers and satellites [Lopatin et al., 2013;

511 Kokhanovsky et al., 2015; Bovchaliuk et al., 2016; Fedarenka et al., 2016; Benavent-

512 Oltra et al., 2017], but not with sky cameras until now. Another important advantage of

513 GRASP is that it is open-source and free (available at www.grasp-open.com).

514 4.1- Forward model

515   GRASP has two main independent modules. One of them is the forward model,

516 which allows the simulation of various atmospheric observations [Dubovik et al., 2014].

517 In this work, this module has been used to simulate the lunar normalized radiance at the

518 same points that were obtained with the camera. Aerosol properties obtained from

519 AERONET have been used as inputs to make these simulations of normalized radiance

520 on the lunar almucantar for the three camera effective wavelengths. For a given night, the

521 nearest AERONET aerosol inversion of the previous afternoon or the next morning has

522 been chosen. The AERONET aerosol properties used from this inversion have been: 22-

523 bin volume size distribution (logarithmically spaced), real and imaginary refractive

524 indices at four wavelengths, and sphere fraction. In order to obtain the radiance at the

525 camera wavelengths the refractive indices at these wavelengths is needed; therefore the

526 refractive indices at 469, 533 and 608 nm have been calculated using a linear interpolation

527 of the AERONET available values. All these aerosol properties and, in addition, the MZA

25

528   have been introduced into GRASP forward model. The output of the model has given the

529   normalized radiance in the lunar almucantar at 469 nm, 533 nm and 608 nm.

530   **4.2- Aerosol retrieval**

531   The main module of GRASP is the numerical inversion, which includes general

532   mathematical operations not related to the particular physical nature of the inverted data

533   [Dubovik et al., 2014]. This module, in combination with the forward module, can

534   retrieve aerosol properties from a data set of atmospheric measurements. GRASP is

535   configured to process absolute radiances but also normalized radiances. The inverted data

536   set in this work, used as input in GRASP, have been six values of AOD (440, 500, 675,

537   870, 1020, and 1640 nm) from CE318-T photometer and the normalized radiance from

538   the camera at 469 nm, 533 nm and 608 nm at 36 points per wavelength (lunar almucantar

539   points from 183º to 200º every 1º). A bilognormal size distribution has been selected in

540   order to represent the retrieved size distribution (instead of the 22-bin representation used

541   in AERONET), and different smoothness and "a priori" constraints on the aerosol size

542   distribution have been applied [Dubovik et al., 2014]. Aerosol refractive indices, both real

543   (RRI) and imaginary (IRI), have been assumed as constant (non spectral variation); this

544   assumption has been done due to the lack of information regarding the diurnal retrievals

545   which consider that refractive indices can vary with wavelength.

546   As a result, for each HDR image and 6-AOD dataset, the following parameters have been

547   obtained: bilognormal size distribution, real and imaginary refractive indices, single

548   scattering albedo (SSA) at the same wavelengths than input values, and sphere fraction.

549   The retrieved bilognormal size distribution is described by six independent parameters

550   [Torres et al., 2016]: volume concentration of the fine (C_f) and coarse mode (C_c); volume

551   median radius of the fine (r_f) and coarse mode (r_c), and geometric standard deviation for

552   both modes: σ_f (fine) and σ_c (coarse). This geometric standard deviation is related to the

553   width of the size distribution centered in the median radius.

554

5- Results

555

5.1- Camera radiances versus simulations

556

557   As described in the introduction, the first step will be the validation of the

558   normalized radiances obtained with the sky camera. For this purpose, the lunar

559   almucantars obtained from the camera and their equivalent simulated with the GRASP

560   forward model have been compared on different nights.

561   **5.1.1- Individual case**

562   A desert dust plume was detected at Granada during the evening of 20th July 2016.

563   The ceilometer signal (not shown) indicated that it arrived in Granada at around 15:00

564   UTC. The AERONET values of Table 1 point out the presence of desert dust after 15:00

565   UTC: Angström Exponent at 17:55 UTC was 0.2, indicating coarse particle

566   predominance with a strong AOD at 440 nm of 0.98. The AOD along the night (not

567   shown) did not present significant changes and the AERONET retrieval at the next

568   morning (not shown) is similar to the one shown in Table 1. Therefore, the aerosol

569   characteristics did not present relevant variations along the night from 20th to 21st July

570   2016. That night the Moon Phase Angle (MPA) was 13º at midnight (one day after full

571   Moon), therefore with a large Moon irradiance associated. The normalized radiance at

572   lunar almucantar geometry has been obtained from the sky camera at various night times.

573   The radiance has also been simulated at the same times using as input the AERONET

574 aerosol optical properties obtained the afternoon of 20th July at 17:55 UTC (Table 1) and

575 the size distribution (not shown in Table 1).

576 Table 1: Retrieved aerosol optical properties from AERONET sunphotometer (level 1.5) near to the
577 previous sunset or the following sunrise for eight nights.

Properties	Wavelength (nm)	29 May 2015 07:45 UTC	3 Aug 2015 06:43 UTC	21 Feb 2016 15:35 UTC	19 May 2016 06:27 UTC	20 May 2016 18:03 UTC	24 May 2016 09:24 UTC	20 July 2016 17:55 UTC	24 July 2016 06:37 UTC
Place	-	Valladolid	Valladolid	Valladolid	Granada	Granada	Granada	Granada	Granada
Photometer ID		#788	#788	#383	#918	#918	#918	#918	#918
Real RI	440	1.39	1.44	1.50	1.35	1.45	1.45	1.42	1.33
	675	1.41	1.44	1.48	1.36	1.44	1.45	1.44	1.34
	870	1.42	1.44	1.47	1.37	1.45	1.45	1.44	1.37
	1020	1.42	1.43	1.46	1.38	1.43	1.44	1.41	1.37
Imaginary RI	440	0.0035	0.0073	0.0035	0.0106	0.0093	0.0053	0.0038	0.0055
	675	0.0030	0.0031	0.0008	0.0082	0.0073	0.0017	0.0010	0.0049
	870	0.0029	0.0029	0.0005	0.0085	0.0073	0.0014	0.0008	0.0053
	1020	0.0029	0.0031	0.0005	0.0083	0.0071	0.0013	0.0007	0.0054
AOD	440	0.20	0.27	1.84	0.21	0.23	0.36	0.98	0.22
	675	0.09	0.20	1.82	0.10	0.11	0.31	0.93	0.11
	870	0.07	0.18	1.75	0.07	0.08	0.30	0.89	0.09
	1020	0.05	0.17	1.70	0.05	0.06	0.29	0.85	0.07
Angström Exponent	440-870	1.6	0.6	0.1	1.7	1.5	0.3	0.2	1.4
Sphere fraction (%)	-	97	3	0	97	98	1	0	94

578

579 Figure 9a shows the obtained camera almucantar for the image of Fig. 6g for

580 Granada on 20th July 2016 at 00:40 UTC. This almucantar is similar to the simulated one

581 (Fig. 9b), both showing the highest radiances near the Moon at 469 nm, followed by 533

582 nm. Finally for this case, the ratio between the camera and the simulated normalized

583 radiances has been represented in Fig. 9c as a function of azimuth for different HDR

584 images taken that night. This ratio presents values near to 1 for all wavelengths, except

585 for the highest azimuth values where the ratio fluctuates especially for 469 nm. These

586 results indicate a good agreement between measurements and simulations for this case.
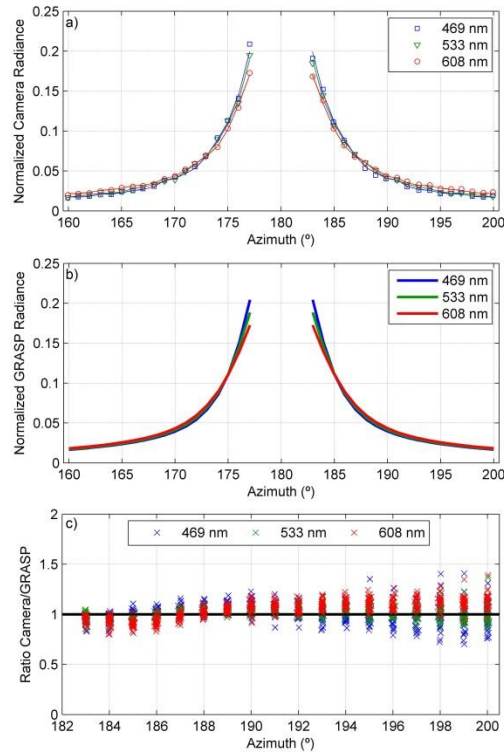
Figure 9: Normalized lunar almucantar radiances from camera (panel a) and simulated ones by GRASP (panel b) for Granada 21st July 2016, 00:40UTC. Panel c shows the ratio of normalized camera radiance to normalized GRASP radiance along the night 20th-21st May 2016 as a function of azimuth.

5.1.2- Statistical analysis

In addition to the analyzed case, seven other nights have been added to the dataset for comparison, with a total of 8 nights (4 cases with fine aerosol predominance and 4 coarse aerosol cases), 5 at Granada and 3 at Valladolid. The normalized radiances have been simulated for the eight nights as in the previous case using the parameters of the AERONET retrievals (corresponding to the afternoon before or to the morning after) shown in Table 1. Clean cases (low aerosol load) have not been considered due to the uncertainties in the aerosol parameters under low aerosol load. In fact, the aerosol parameters retrieved by AERONET present quality assurance only when the AOD at 440 nm is higher than 0.4 [Holben et al., 2006]; however, due to the lack of coincident cases with high AOD values and camera measurements under stable and constant aerosol conditions along a full night, AERONET data used were retrieved with AOD at 440 nm

603   higher than 0.2, with only two cases of AOD at 440 nm above 0.4 (related to coarse

604   particle events).

605   Figure 10 shows the scatter plots (one per wavelength) of normalized camera

606   radiance against simulated radiances for the eight nights. The aerosol type of each night

607   is also available at Table 2. The normalized camera radiances show a high correlation

608   with the simulated one for all nights, but normalized radiance at 469 nm presents the

609   largest deviation. Some of the cases present high normalized radiances due to a lack in

610   the number of data in the lunar almucantar caused by the criteria explained in Section

611   3.2.4: Moon intensity likely too low (near quarters). If the number of points of lunar

612   almucantar decreases, the normalized radiance values increase.
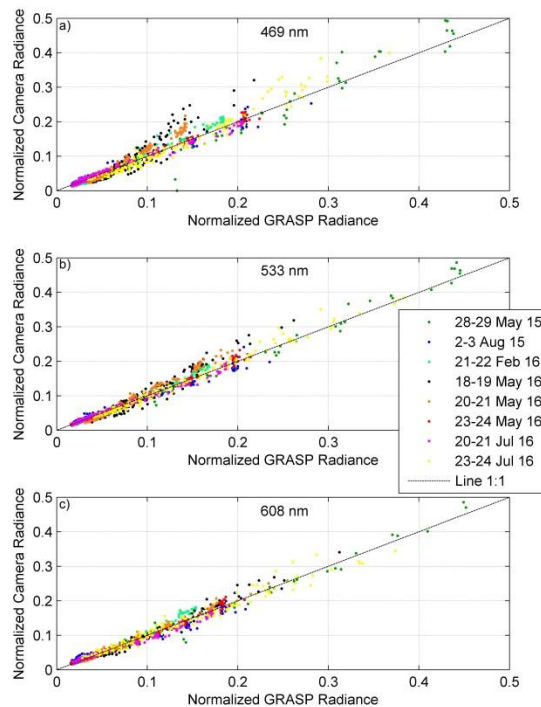
613

614   Figure 10: Normalized radiance from camera as a function of simulated by GRASP for 8 different nights
615   at 469 nm (panel a), 533 nm (panel b) and 608 nm (panel c).

616   Table 2 shows the slope, y-intercept and determination coefficient of the least

617   squares fit between camera and simulated radiances. A large correlation is observed, with

618   r^2 values above 0.90 for all cases, the fine aerosol cases presenting the lowest correlation.

619   From all the cases, the values at 469 nm have the lowest correlation but the overall r^2 is

620   still high at 0.96. The slope of the fit frequently indicates that the values from the camera

621   overestimate the simulations for shorter wavelengths. The y-intercept values usually

622   decrease in absolute value with wavelength, being farther from zero for the fine aerosol

623   cases, especially at 469 and 533 nm. When all the analyzed nights are considered together,

624   the fit slope shows that camera radiance overestimates around 6% and 3% the simulations

625   at 469 and 533 nm, respectively, being the slope equal to 1.00 for 608 nm. These results

626   point out that normalized camera radiance is in good agreement with the simulated

627   radiance, especially at 608 nm.

628

629   Table 2: Statistical parameters of the scatter plots of normalized camera radiance against simulated one
630   for three wavelengths and different cases. N is the number of available data pairs for each wavelength.

| Case (Type) | Wavelength (nm) | | | | | | | | | | | |
| | 469 | | | | 533 | | | | 608 | | | |
	N	Slope	y-intercept	r^2	N	Slope	y-intercept	r^2	N	Slope	y-intercept	r^2
Valladolid 28-29 May 2015 (Fine)	43	1.16	-0.0490	0.93	36	1.03	-0.0100	0.99	42	1.03	-0.0082	0.99
Valladolid 2-3 August 2015 (Coarse)	275	0.94	0.0034	0.98	281	0.90	0.0054	0.98	285	0.88	0.0070	0.98
Valladolid 21-22 Feb 2016 (Coarse)	522	1.12	-0.0064	0.99	522	1.05	-0.0028	0.99	522	1.09	-0.0049	0.98
Granada 18-19 May 2016 (Fine)	275	1.51	-0.0349	0.90	232	1.29	-0.0236	0.96	228	1.10	-0.0086	0.98
Granada 20-21 May 2016 (Fine)	502	1.48	-0.0268	0.99	464	1.29	-0.0176	0.99	462	1.06	-0.0035	0.99
Granada 23-24 May 2016 (Coarse)	299	1.03	-0.0016	1.00	294	1.02	-0.0009	0.99	297	0.99	-0.0005	0.99
Granada 20-21 July 2016 (Coarse)	504	0.95	0.0025	0.99	504	0.97	0.0019	1.00	504	0.90	0.0057	0.99
Granada 23-24 July 2016 (Fine)	154	1.18	-0.0232	0.97	141	1.05	-0.0075	0.99	158	0.96	0.0046	0.97
All	2574	1.06	-0.0042	0.96	2474	1.03	-0.0020	0.99	2498	1.00	-0.0001	0.99

631

632   For an in-depth analysis, the relative differences (ΔNR) between the camera and

633   simulations have been calculated for each night, image and channel as:

634
$$\Delta NR(\%) = 100\% \frac{NCR - NGR}{NGR} \tag{3}$$

635   where NCR is the normalized radiance of the camera and NGR (normalized GRASP

636   radiance) the simulated one. ΔNR has been calculated using all available data and its

637   distribution is shown for different azimuth angle intervals in Fig. 11. The green channel

638   presents the lowest changes on bias (mean of ΔNR) being near zero for all azimuth values,

639   while for high azimuth values the camera measurements over/under-estimates the

640   simulations near the Moon at blue/red channel. These bias values are also shown in Table

641   3, ranging from -3.2% (469 nm) to 1.5% (608 nm) when all azimuth values are

642   considered. The standard deviation (σ) increases with azimuth and the highest values are

643   found for 469 nm. The standard deviation can be assumed as the uncertainty if the ΔNR

644   distribution is Gaussian, which implies that the percentage of ΔNR data (absolute value)

645   lower than standard deviation (P<σ) must be about 68%, and the percentage of ΔNR data

646   (absolute value) lower than two standard deviations (P<2σ) must be around 95% [Román

647   et al., 2014a].
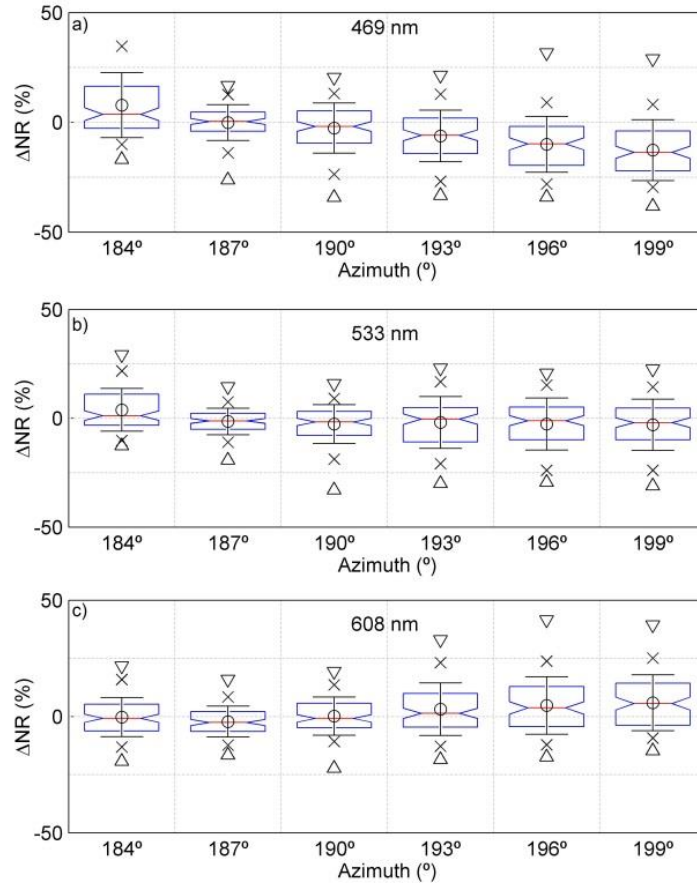
Figure 11: Box plots for the relative distribution of ΔNR at 469 nm (panel a), 533 nm (panel b) and 608 nm (panel c) for different azimuth intervals. The box limits are the 25 and 75 percentiles, the error bar is the standard deviation, the circle is the mean, the red line inside the box is the median, the crosses are the 5 and 95 percentiles, and the triangles are the 1 and 99 percentiles.

Table 3 presents the values of P<σ and P<2σ, which are close to 68% and 95% for all cases, especially for 533 and 608 nm, hence the standard deviation can be considered as the uncertainty of the normalized camera radiance. Then, uncertainty for azimuth intervals from 182.5º to 191.5º falls within 8%-15%, 6%-10% and 7%-8% for 469 nm, 573 nm and 608 nm, respectively. The obtained uncertainty considering all data at each channel (~2500 data) is 14%, 10% and 10% for 469 nm, 533 nm and 608 nm, respectively. In general the fit between measurements and simulations is similar for the green and red channels and slightly worse for the blue channel.

Table 3: Statistical estimators of ΔNR for different azimuth intervals and three wavelengths. N is the number of data used; σ is the standard deviation, RMSE is the root mean square difference between camera and simulated radiances; P<σ is the percentage of ΔNR values inside the interval (-σ, σ); and P<2σ is the percentage of ΔNR values inside the interval (-σ, 2σ).

	Wavelength (nm)	Azimuth interval (°)						
		182.5-185.5	185.5-188.5	188.5-191.5	191.5-194.5	194.5-197.5	197.5-200.5	182.5-200.5
N	469	505	475	438	399	389	368	2574
	533	501	468	429	392	358	326	2474
	608	499	475	437	390	366	331	2498
Mean (%)	469	7.85	-0.08	-2.61	-6.23	-10.02	-12.67	-3.21
	533	3.87	-1.47	-2.63	-1.92	-2.64	-2.94	-1.02
	608	-0.29	-2.19	0.19	3.15	4.73	5.92	1.53
Median (%)	469	3.73	0.42	-1.83	-5.85	-9.78	-13.64	-3.06
	533	1.26	-1.20	-1.66	-0.35	-1.08	-2.00	-0.60
	608	-0.73	-2.54	-0.81	1.39	3.70	5.60	0.17
σ (%)	469	14.84	8.15	11.40	11.73	12.71	13.91	14.06
	533	9.83	6.07	8.87	11.92	11.98	11.72	10.38
	608	8.42	6.61	8.23	11.32	12.39	12.00	10.19
P<σ (%)	469	70.30	74.95	73.74	59.90	52.19	47.83	71.10
	533	66.47	71.58	73.89	67.60	66.48	69.94	72.39
	608	69.14	69.05	72.54	71.28	68.85	66.77	73.66
P<2σ (%)	469	90.69	94.53	93.84	91.23	89.20	91.58	94.76
	533	93.01	94.44	93.47	96.43	94.69	94.17	93.98
	608	95.79	94.97	94.97	94.10	96.17	93.05	95.56

The obtained results have been calculated using the eight nights simulated with the properties of Table 1. However, only two retrievals of Table 1 satisfy the criteria of quality assurance of AERONET at 440 nm; then if the same analysis is done for all azimuth values with only these two cases, the uncertainty of the normalized camera radiance decreases to 11%, 6% and 9% for 469 nm, 533 nm and 608 nm, respectively. These uncertainty values range between 5%-14% (469 nm), 4%-7% (533 nm) and 6%-9% (608 nm) for the different azimuth intervals.

The ΔNR distribution has been represented for different MZA intervals in Fig. 12. The best agreement between camera and simulations appears at MZA values from 30° to 40°, as percentile 5 and 95 indicate for all wavelengths, but this behavior is not significant since only one of the eight nights analyzed reached these low MZA values. The mean, median and standard deviation values do not show a clear dependence on MZA. The values of P<σ and P<2σ (Table 4) show that the standard deviation can be considered the

679   uncertainty of the normalized camera radiances, and the lowest values of this uncertainty

680   are for 30º-40º interval (5%-7%), followed by 60-70º interval (8%-14%). The worse

681   agreement appears for the largest MZA values, which could be due to the stronger

682   background light at these angles.
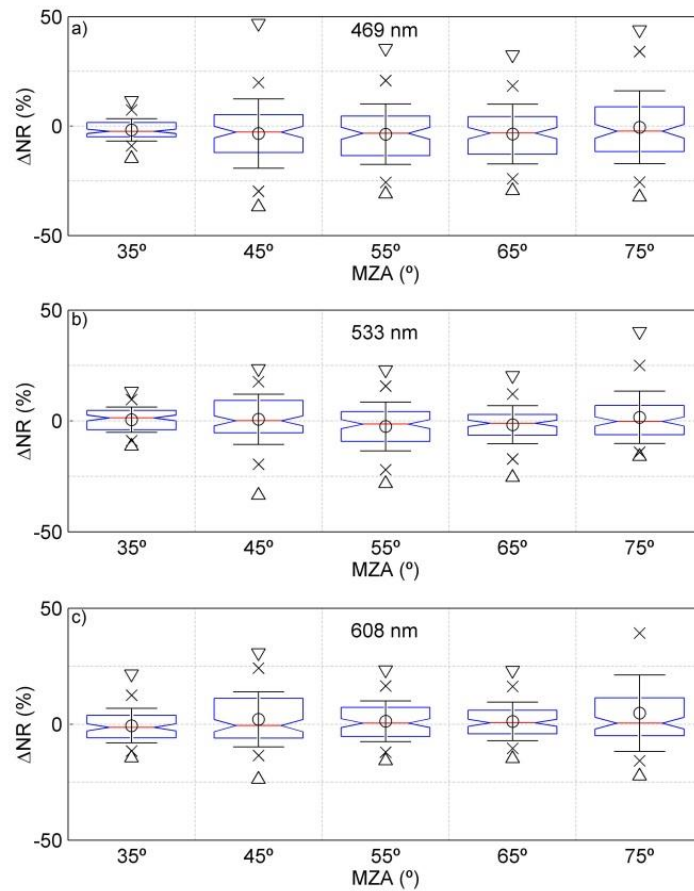
683

684   Figure 12: Box plots for the relative distribution of ΔNR at 469 nm (panel a), 533 nm (panel b) and 608
685   nm (panel c) for different MZA intervals. The box limits are the 25 and 75 percentiles, the error bar is the
686   standard deviation, the circle is the mean, the red line inside the box is the median, the crosses are the 5
687   and 95 percentiles, and the triangles are the 1 and 99 percentiles.

688   Table 4: Statistical estimators of ΔNR for different MZA intervals and three wavelengths. N is the
689   number of data used; σ is the standard deviation, RMSE is the root mean square difference between
690   camera and simulated radiances; P<σ is the percentage of ΔNR values inside the interval (-σ, σ); and
691   P<2σ is the percentage of ΔNR values inside the interval (-2σ, 2σ).

	Wavelength (nm)	MZA interval (º)				
		30-40	40-50	50-60	60-70	70-80
	469	216	590	970	596	202
N	533	216	562	944	561	191
	608	216	578	962	554	188
	469	-1.75	-3.42	-3.70	-3.64	-0.53

Mean (%)	533	0.51	0.71	-2.51	-1.74	1.60
	608	-0.64	2.08	1.26	1.18	4.72
Median (%)	469	-2.37	-2.75	-3.30	-3.21	-2.30
	533	1.36	0.07	-1.42	-1.06	-0.21
	608	-1.37	-0.61	0.50	0.62	0.46
σ (%)	469	5.09	15.85	13.84	13.70	16.64
	533	5.70	11.32	10.97	8.62	11.78
	608	7.46	11.88	8.76	8.28	16.48
P< σ (%)	469	67.59	72.03	67.32	68.79	69.80
	533	63.43	70.28	69.70	73.44	75.39
	608	73.15	68.86	67.88	72.74	81.91
P<2σ (%)	469	94.91	93.90	94.95	96.48	93.07
	533	97.69	94.66	93.64	93.23	94.76
	608	95.37	93.60	96.26	94.77	93.09

692

5.2- Retrieval of aerosol properties

694   A desert dust event arrived at Valladolid the night from 2nd to 3rd August 2015.

695 Figure 13 shows the AOD and Angström Exponent on both days during the day-night

696 period. The aerosol load during 2nd August was low, with an AOD at 440 nm close to 0.1

697 during all day and Angström Exponent about 1.5, indicating fine mode predominance.

698 However, at the beginning of the next day, the AOD at 440 nm was about three times

699 higher and the Angström Exponent was 0.5 (indicating coarse particle predominance).

700 The night time measurements of the CE318-T photometer show that about 22:30 UTC

701 the AOD started to increase while Angström Exponent began to decrease; indicating the

702 dust plume outbreak. Ceilometer profiles and back-trajectories (not shown) confirm the

703 Saharan dust outbreak that night.
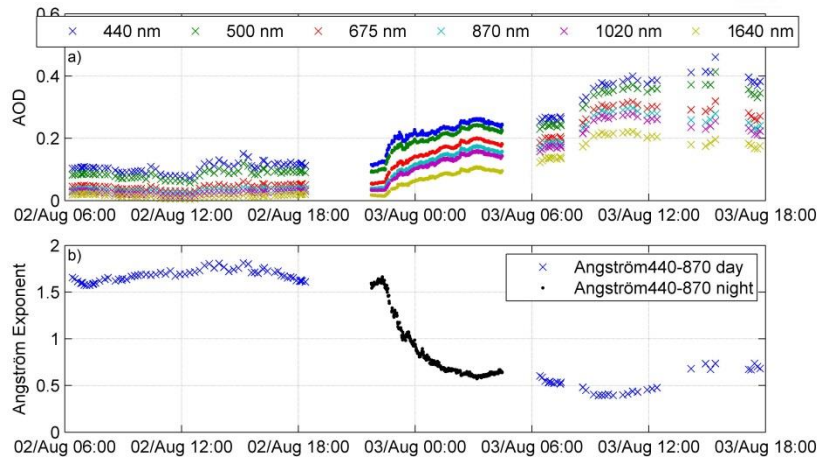
704

Figure 13: Spectral AOD (panel a) and Angström Exponent (panel b) at day and night from 2nd to 3rd August 2015 at Valladolid. Crosses and points represent nocturnal and diurnal data, respectively.

The normalized radiance obtained from the SONA camera has been calculated for that night and it has been used as input in GRASP together with the 6 spectral AOD measurements derived from direct lunar observations, as commented in Section 4.2. The GRASP retrievals for that night have been run every 15 minutes, but there is a lack of data around midnight when the camera was not operative. One of the HDR images used in this analysis is the one shown in Fig. 6i. Figure 14 shows the retrieved real (panel a) and imaginary refractive (panel b) indices, sphere fraction (panel c) and SSA values (panel d). The previous and next daytime AERONET values are also included in the graphs. Real part of refractive index presented values around 1.40 and 1.49 and with an error bar that fits with the diurnal AERONET retrievals. The imaginary part of the refractive index shows more fluctuations along the night and with a large error bar; the most IRI values are low once the dust aerosol appeared, as the AERONET value of the next morning. Sphere fraction also shows the dust intrusion in the night since at the beginning of the night the aerosols were mainly spherical but they progressively changed to predominance of non-spherical particles, i.e. desert dust. These changes can be also appreciated in the wavelength dependence of SSA, since at the beginning of the night the

723   SSA was higher for shorter wavelengths but this fact changed with the dust intrusion,

724   which typically presents lower SSA values for shorter wavelengths.
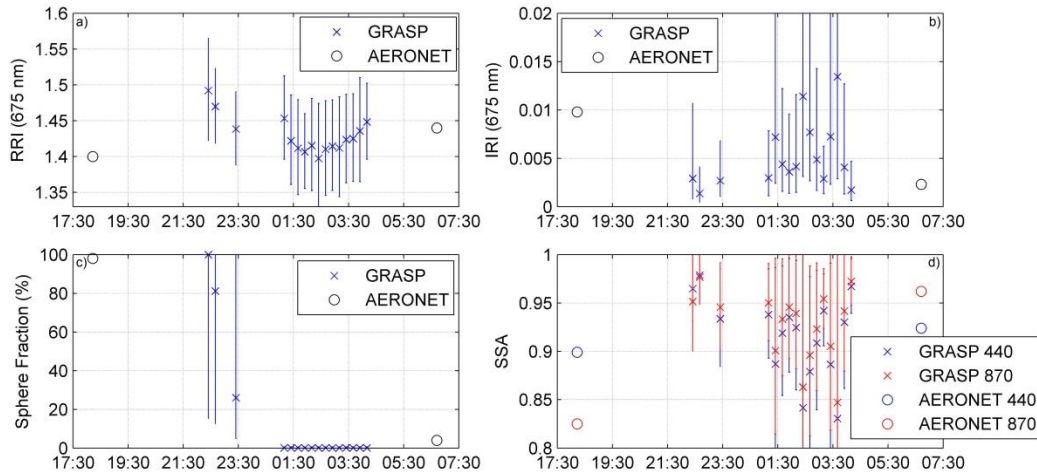
725

726   Figure 14: Evolution of the real (panel a) and imaginary (panel b) refractive indices, sphere fraction
727   (panel c) and SSA (panel d) at Valladolid from 2nd to 3rd August 2015. Diurnal values retrieved by
728   AERONET are represented as circles, while nocturnal values retrieved by GRASP, using normalized
729   camera radiances and nocturnal AOD, are represented by crosses with their error bars.

730   Regarding the volume size distribution, Figure 15 shows the volume median

731   radius (panels a and b), the geometric standard deviation (panels c and d) and the volume

732   concentration (panels e and f) for both fine and coarse modes. Diurnal retrieved values

733   from AERONET are also included. Regarding the fine mode, the properties do not present

734   strong changes along the night, being similar the retrieved (night time) properties and the

735   AERONET ones. The r_c values decreased along the night being centered around 2 µm

736   after midnight; this variation is in agreement with the AERONET data. Volume

737   concentration of the coarse mode, V_c, is also in agreement with the AERONET values

738   since it presented values around 0.03 $\mu m^3/\mu m^2$ at the beginning of the night and this

739   concentration raised up to around 0.1 $\mu m^3/\mu m^2$ at the end of the night. The geometric

740   standard deviation values of coarse mode σ_c obtained by GRASP are higher than the

741   nearest AERONET product, which indicates that the coarse mode of the size distribution

742   was wider at night.
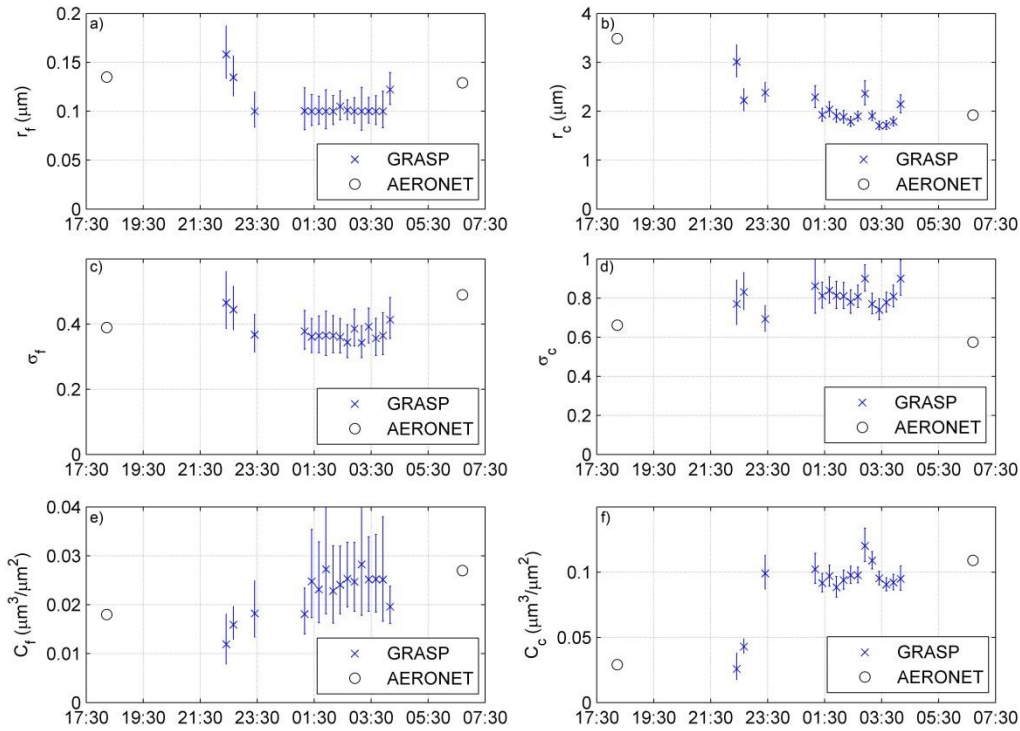
743

Figure 15: Parameters of the fine (panels a, c and e) and coarse (panels b, d and f) aerosol size
distributions from AERONET (black circles) and from GRASP retrieval using normalized
camera radiances and nocturnal AOD (blue crosses with error bars) at Valladolid from 2nd to 3rd
August 2015.

6- Conclusions

Normalized radiances around lunar aureole can be measured with a sky camera if it is configured to capture HDR images. Lunar almucantars from the camera have been compared with simulated radiances, obtaining a better fit between camera and model when the aerosol load is high and the Moon light is bright enough. The uncertainty of normalized camera radiance gets higher as the azimuth value goes farther from the Moon. This uncertainty is lower for MZA values from 30° to 40°, but it does not present a clear dependence on MZA. The camera normalized radiance uncertainty is 10% with an absolute bias around 1.0% and 1.5% for green and red channels, while the uncertainty of blue channel is 14% with an absolute bias of -3.2%. In general, the normalized camera radiances fits the simulations better for the green (533 nm) and red (608 nm) channels.

760 GRASP code has the capability to include normalized radiances in the aerosol

761 retrievals. The inversion of nocturnal AOD and normalized camera radiances together

762 with GRASP could be used to study the aerosol properties evolution along the night, as

763 it has been observed for a dust outbreak episode at Valladolid. In general, the obtained

764 aerosol properties by GRASP at night fit well with the nearest diurnal properties provided

765 by AERONET.

766 This work has demonstrated that normalized radiance near the lunar aureole can

767 be detected by a sky camera, but, as a future work, the use of these normalized radiances

768 in GRASP will need an exhaustive sensitivity study in order to ascertain which lunar

769 aureole points provide more information, what aerosol properties can be retrieved with

770 enough accuracy using this kind of measurements, and what are the best retrieval

771 constraints.

772

773

774

775

776

777

778

779

796

797

798

799

800

801

802   **References**

803 Alonso, J., Batlles, F.J., López, G., Ternero, A. (2014): Sky camera imagery processing
804 based on a sky classification using radiometric data. Energy, 68, 599-608.

805 Ansmann, A., Riebesell, M., and Weitkamp, C. (1990): Measurement of atmospheric
806 aerosol extinction profiles with a Raman lidar. Opt. Lett. 15, 746–748.

807 Ansmann, A., Wagner, F., Althausen, D., Müller, D., Herber, A., and Wandinger, U.
808 (2001): European pollution outbreaks during ACE 2: Lofted aerosol plumes observed
809 with Raman lidar at the Portuguese coast. J. Geophys. Res., 106, 20725–20733.

810 Barreto, A., Cuevas, E., Damiri, B., Berkoff, T., Berjón, A.J., Hernández, Y., Almansa,
811 F., Gil, M. (2013): A new Method for nocturnal aerosol measurements with a lunar
812 photometer prototype. Atmos. Meas. Tech., 6, 585–598.

813 Barreto, A., Cuevas, E., Granados-Muñoz, M.J., Alados-Arboledas, L., Romero, P.M.,
814 Gröbner, J., Kouremeti, N., Almansa, A.F., Stone, T., Toledano, C., Román, R., Sorokin,
815 M., Holben, B., Canini, M., Yela, M. (2016): The new sun-sky-lunar Cimel CE318-T
816 multiband photometer – a comprehensive performance evaluation. Atmos. Meas. Tech.,
817 9, 631–654.

818 Barreto, A., Román, R. Cuevas, E., Berjón, A.J., Almansa, A.F., Toledano, C., González,
819 R., Hernández, Y., Blarel, L., Goloub, P., Yela, M. (2017): Assessment of nocturnal
820 Aerosol Optical Depth from lunar photometry at Izaña high mountain Observatory.
821 Atmos. Meas. Tech. Discuss., doi:10.5194/amt-2016-423.

822 Benavent-Oltra, J.A., Román, R., Granados-Muñoz, M.J., Pérez-Ramírez, D., Ortiz-
823 Amezcua, P., Denjean, C., Lopatin A., Lyamani, H., Torres, B., Guerrero-Rascado, J. L.,
824 Fuertes, D., Dubovik, O., Chaikovsky, A., Olmo, F.J., Mallet, M., Alados-Arboledas, L.
825 (2017): Validation of GRASP code for a dust event over Granada (Spain) during
826 ChArMEx/ADRIMED 2013 campaign. Submitted to Atmos. Chem. Phys.

827 Berkoff, T.A., Sorokin, M., Stone, T., Eck, T.F., Hoff, R., Welton, E., Holben, B. (2011):
828 Nocturnal aerosol optical depth measurements with a small-aperture automated
829 photometer using the moon as a light source. J. Atmos. Ocean. Tech., 28, 1297–1306,
830 doi:10.1175/JTECH-D-10-05036.1.

831 Bovchaliuk, V., Goloub, P., Podvin, T., Veselovskii, I., Tanre, D., Chaikovsky, A.,
832 Dubovik, O., Mortier, A., Lopatin, A., Korenskiy, M., Victori, S. (2016): Comparison of
833 aerosol properties retrieved using GARRLiC, LIRIC, and Raman algorithms applied to
834 multi-wavelength LIDAR and sun/sky-photometer data. Atmos. Meas. Tech., 9, 3391-
835 3405.

836 Cachorro, V.E., Burgos, M.A., Mateos, D., Toledano, C., Bennouna, Y., Torres, B., de
837 Frutos, A., Herguedas, A. (2016). Inventory of African desert dust events in the north-
838 central Iberian Peninsula in 2003–2014 based on sun-photometer–AERONET and
839 particulate-mass–EMEP data. Atmos. Chem. Phys., 16(13), 8227-8248.

840 Calbó, J., Sabburg, J. (2008): Feature extraction from whole-sky ground-based images
841 for cloud-type recognition. Journal of Atmospheric and Oceanic Technology, 25(1), 3-
842 14.

843 Cazorla, A., Olmo, F.J., Alados-Arboledas, L. (2008a). Development of a sky imager for
844 cloud cover assessment. J. Opt. Soc. Am. A, 25(1), 29-39.

845 Cazorla, A., Olmo, F.J., Alados-Arboledas, L. (2008b): Using a Sky Imager for aerosol
846 characterization. Atmos. Environ., 42, 2739–2745, doi:10.1016/j.atmosenv.2007.06.016.

847 Cazorla, A., Husillos, C., Antón, M., Alados-Arboledas, L. (2015): Multi-exposure
848 adaptive threshold technique for cloud detection with sky imagers. Solar Energy 114,
849 268–277.

850 Cazorla, A., Casquero-Vera, J.A., Román, R., Guerrero-Rascado, J.L., Toledano, C.,
851 Cachorro, V.E., Orza, J.A.G., Cancillo, M.L., Titos, G., Pandolfi, M., Alastuey, A.,
852 Hanrieder, N., Alados-Arboledas, L. (2017): Near real time processing of ceilometer
853 network data: Characterizing an extraordinarty dust outbreak over the Iberian Peninsula.
854 Atmos. Chem. Phys. Discuss., doi:10.5194/acp-2017-151.

855 Chauvin, R., Nou, J., Thil, S., Grieu, S. (2015): Modelling the clear-sky intensity
856 distribution using a sky imager. Solar Energy, 119, 1-17.

857 Debevec, P.E., Malik, J. (1997): Recovering high dynamic range radiance maps from
858 photographs. Proceedings of SIGGRAPH 97, 369–378. ISBN 0-89791-896-7. Held in
859 Los Angeles, California.

860 Dubovik, O., King, M. D. (2000): A flexible inversion algorithm for retrieval of aerosol
861 optical properties from Sun and sky radiance measurements. J. Geophys. Res. Atmos.,
862 105, 20673–20696.

863 Dubovik, O., Smirnov, A., Holben, B.N., King, M.D., Kaufman, Y.J., Eck, T.F., Slutsker,
864 I. (2000): Accuracy assessments of aerosol optical properties retrieved from Aerosol
865 Robotic Network (AERONET) Sun and sky radiance measurements. Journal of
866 Geophysical Research: Atmospheres, 105(D8), 9791-9806.

867 Dubovik, O., Sinyuk, A., Lapyonok, T., Holben, B.N., Mishchenko, M., Yang, P., Eck,
868 T., Volten, H., Munoz, O., Veihelmann, B., Van Der Zande, W.J., Leon, J., Sorokin, M.,
869 Slutsker, I. (2006): Application of spheroid models to account for aerosol particle
870 nonsphericity in remote sensing of desert dust. J. Geophys. Res. Atmos., 111, D11208.

871 Dubovik, O., Lapyonok, T., Litvinov, P., Herman, M., Fuertes, D., Ducos, F., Lopatin,
872 A., Chaikovsky, A., Torres, B., Derimian, Y., Huang, X., Aspetsberger, M., Federspiel,
873 C. (2014): GRASP: a versatile algorithm for characterizing the atmosphere. SPIE:
874 Newsroom 10.1117/2.1201408.005558.

875 Fedarenka, A., Dubovik, O., Goloub, P., Li, Z., Lapyonok, T., Litvinov, P., Blarel, L.,
876 Gonzalez, L., Podvin, T., Crozel, D. (2016): Utilization of AERONET polarimetric

877   measurements for improving retrieval of aerosol microphysics: GSFC, Beijing and Dakar
878   data analysis. J. Quant. Spectrosc. Radiat. Transfer, 179, 72-97.

879   Fernald F.G. (1984): Analysis of atmospheric lidar observations: some comments. Appl.
880   Opt. 23, 652–653.

881   Forster, B.C., Best, P. (1994): Estimation of SPOT P-mode point spread function and
882   derivation of a deconvolution filter. ISPRS Journal of Photogrammetry and Remote
883   Sensing, 49(6), 32-42.

884   Ghonima, M.S., Urquhart, B., Chow, C.W., Shields, J.E., Cazorla, A., Kleissl, J. (2012):
885   A method for cloud detection and opacity classification based on ground based sky
886   imagery. Atmos. Meas. Tech., 5(11), 2881-2892.

887   González, Y., Lopez, C., Cuevas, E. (2012): Automatic observation of cloudiness:
888   analysis of all sky images, TECO-2012, In: WMO Technical Conference on
889   Meteorological and Environmental Instruments and Methods of Observation, Brussels,
890   Belgium, 16–18 October 2012.

891   Haywood, J.M., Boucher, O. (2000): Estimates of the direct and indirect radiative forcing
892   due to tropospheric aerosols: A review. Rev. Geophys., 38, 513–543.

893   Holben, B.N., Eck, T.F., Slutsker, I., Tanré, D., Buis, J.P., Setzer, A., Vermote, E.,
894   Reagan, J. A., Kaufman, Y. J., Nakajima, T., Lavenu, F., Jankowiak, I., Smirnov A.
895   (1998): AERONET – A federated instrument network and data archive for aerosol
896   characterization. Remote Sens. Environ., 66, 1–16, 1998.

897   Holben, B. N., Eck, T. F., Slutsker, I., Smirnov, A., Sinyuk, A., Schafer, J., Giles, D.,
898   Dubovik, O. (2006): AERONET's version 2.0 quality assurance criteria. Proc. SPIE 6408,
899   Remote Sensing of the Atmosphere and Clouds, 64080Q (November 28, 2006);
900   doi:10.1117/12.706524.

901   Horváth, G., Barta, A., Gál, J., Suhai, B., Haiman, O. (2002): Ground-based full-sky
902   imaging polarimetry of rapidly changing skies and its use for polarimetric cloud
903   detection. Appl. Optics, 41, 543–559.

904   IPCC (Intergovernmental Panel on Climate Change) (2014): Climate Change 2014:
905   Synthesis Report. Contribution of Working Groups I, II and III to the Fifth Assessment
906   Report of the Intergovernmental Panel on Climate Change [Core Writing Team, R.K.
907   Pachauri and L.A. Meyer (eds.)]. IPCC, Geneva, Switzerland, 151.

908   Kaufman, Y.J., Koren, I., Remer, L.A., Rosenfeld, D., Rudich, Y. (2005): The effect of
909   smoke, dust, and pollution aerosol on shallow cloud development over the Atlantic
910   Ocean. Proc. Natl. Acad. Sci. USA, 102, 11207–11212.

911   Kazantzidis, A., Tzoumanikas, P., Bais, A.F., Fotopoulos, S., Economou, G. (2012):
912   Cloud detection and classification with the use of whole-sky ground-based images.
913   Atmos. Res., 113, 80-88.

914 Kholopov, G. K. (1975): Calculation of the effective wavelength of a measuring
915 system. J. Appl. Spectrosc., 23, 1146–1147, doi:10.1007/BF00611771.

916 Kieffer, H.H., Stone, T.C. (2005): The spectral irradiance of the moon. Astronom. J., 129,
917 2887–2901.

918 Klett J.D. (1981): Stable analytical inversion solution for processing lidar returns. Appl.
919 Opt. 20, 211–220.

920 Klett J.D. (1985): Lidar inversion with variable backscatter/extinction ratios. Appl. Opt.
921 24, 1638–1643.

922 Kokhanovsky, A.A., Davis, A.B., Cairns, B., Dubovik, O., Hasekamp, O.P., Sano, I.,
923 Mukai, S., Rozanov, V.V., Litvinov, P., Lapyonok, T., Kolomiets, I.S., Oberemok, Y.A.,
924 Savenkov, S., Martin, W., Wasilewski, A., Di Noia, A., Stap, F.A., Rietjens, J., Xu, F.,
925 Natraj, V., Duan, M., Cheng, T., Munro, R. (2015): Space-based remote sensing of
926 atmospheric aerosols: The multi-angle spectro-polarimetric frontier. Earth-Science
927 Reviews, 145, 85-116.

928 Kreuter, A., Zangerl, M., Schwarzmann, M., Blumthaler, M. (2009): All-sky imaging: a
929 simple, versatile system for atmospheric research. Appl. Optics, 48, 1091–1097.

930 Lohmann, U., Feichter, J. (2005): Global indirect aerosol effects: A review. Atmos.
931 Chem. Phys. 5, 715–737.

932 Long, C.M., Sabburg, J.M., Calbó, J., and Pagés, D. (2006): Retrieving cloud
933 characteristics from ground-based daytime color all-sky images. J. Atmos. Ocean. Tech.,
934 23, 633–652.

935 Lopatin, A., Dubovik, O., Chaikovsky, A., Goloub, P., Lapyonok, T., Tanré, D., Litvinov,
936 P. (2013): Enhancement of aerosol characterization using synergy of lidar and sun-
937 photometer coincident observations: the GARRLiC algorithm. Atmos. Meas. Tech., 6,
938 2065–2088, doi:10.5194/amt-6-2065-2013.

939 López-Álvarez, M., Hernández-Andrés, J., Romero, J., Olmo, F.J., Cazorla, A., and
940 Alados-Arboledas, L. (2008): Using a trichromatic CCD camera for spectral skylight
941 estimation. Appl. Optics, 47, 31–38.

942 Lyamani, H., Olmo F.J., Alados-Arboledas, L. (2010): Physical and optical properties of
943 aerosols over an urban location in Spain: seasonal and diurnal variability. Atmos. Chem.
944 Phys., 10, 239–254.

945 Lyamani, H., Olmo, F.J., Foyo, I., Alados-Arboledas, L. (2011): Black carbon aerosols
946 over an urban area in south-eastern Spain: changes detected after the 2008 economic
947 crisis. Atmos. Environ. 45, 6423-6432.

948 Mandat, D., Pech, M., Hrabovsky, M., Schovanek, P., Palatka, M., Travnicek, P., Prouza,
949 M., Ebr, J. (2014): All Sky Camera instrument for night sky monitoring. in Proceedings
950 of the First AtmoHEAD Conference, Saclay, June 10-12, arXiv:1402.4762.

951 McGillem, C. D., Anuta, P. E., Malaret, E., Yu, K. B. (1983): Estimation of a remote
952 sensing system point-spread function from measured imagery. LARS Technical Reports,
953 81.

954 McMurry, P.H. (2000): A review of atmospheric aerosol measurements. Atmospheric
955 Environment 34, 1959–1999.

956 NASA Facts (1999): Clouds and Energy cycle. Technical Report NF-207, NASA,
957 Goddard Space Flight Center, Maryland, USA.

958 O'Neill, N.T., Eck, T.F., Smirnov, A., Holben, B.N., Thulasiraman, S. (2003): Spectral
959 discrimination of coarse and fine mode optical depth. J. Geophys. Res., 108 (D17), 4559.
960 http://dx.doi.org/10.1029/2002JD002975.

961 Pinilla, C., Ariza, F.J., Peláez, J.A (1999), Obtención de la función de dispersión puntual
962 (PSF) en imágenes SPOT convencionales. Teledetección, VIII Spanish Remote Sensing
963 Meeting. Albacete (Spain), 403-406.

964 Pérez-Ramírez, D., Ruiz, B., Aceituno, J., Olmo, F.J., and Alados-Arboledas, L. (2008):
965 Application of Sun/star photometry to derive the aerosol optical depth. Int. J. Remote
966 Sens., 29, 5113–5132, doi:10.1080/01431160802036425.

967 Pérez-Ramírez, D., Lyamani, H., Olmo, F.J., and Alados-Arboledas, L. (2011):
968 Improvements in star photometry for aerosol characterizations. J. Aerosol Sci., 42, 737–
969 745, doi:10.1016/j.jaerosci.2011.06.010.

970 Ramanathan, V., Cess, R.D., Harrison, E.F., Minnis, P., Barkstrom, B.R. (1989): Cloud
971 radiative forcing and climate: results from the Earth radiation budget experiment.
972 Science, 243(4887), 57.

973 Ramanathan, V., Crutzen, P.J., Kiehl, J.T., Rosenfeld, D. (2001): Atmosphere—Aerosols,
974 climate, and the hydrological cycle. Science, 294, 2119–2124.

975 Reinhard, E., Stark, M., Shirley, P., Ferwerda, J. (2002). Photographic tone reproduction
976 for digital images. ACM Transactions on Graphics (TOG), 21(3), 267-276.

977 Richardson, W.H. (1972): Bayesian-Based Iterative Method of Image Restoration. J. Opt.
978 Soc. Am., 62 (1), 55–59. doi:10.1364/JOSA.62.000055.

979 Lucy, L.B. (1974): An iterative technique for the rectification of observed distributions.
980 Astron. J., 79 (6), 745–754. doi:10.1086/111605.

981 Rodríguez, S., Alastuey, A., and Querol, X. (2012): A review of methods for long term
982 in situ characterization of aerosol dust. Aeolian Res., 6, 55–74,
983 doi:10.1016/j.aeolia.2012.07.004.

984 Román, R., Antón, M., Cazorla, A., de Miguel, A., Olmo, F.J., Bilbao, J., Alados-
985 Arboledas, L. (2012): Calibration of an all-sky camera for obtaining sky radiance at three
986 wavelengths. Atmos. Meas. Tech., 5, 2013–2024.

987 Román, R., Bilbao, J., and de Miguel, A. (2014a): Reconstruction of six decades of daily
988 total solar shortwave irradiation in the Iberian Peninsula using sunshine duration records.
989 Atmos. Environ., 99, 41–50.

990 Román, R., Bilbao, J., and de Miguel, A. (2014b): Uncertainty and variability in satellite-
991 based water vapor column, aerosol optical depth and Angström Exponent, and its effect
992 on radiative transfer simulations in the Iberian Peninsula. Atmos. Environ., 89, 556–569.

993 Rosenfeld, D., Kaufman, Y.J., Koren, I. (2006): Switching cloud cover and dynamical
994 regimes from open to closed Benard cells in response to the suppression of precipitation
995 by aerosols. Atmos. Chem. Phys., 6, 2503–2511.

996 Sasano, Y., Nakane H. (1984): Significance of the extinction/backscatter ratio and the
997 boundary value term in the solution for the two-component lidar equation. Appl. Opt.,
998 vol. 23, 11–13.

999 Sicard, M., Bertolín, S., Mallet, M., Dubuisson, P., Comerón, A. (2014): Estimation of
1000 mineral dust long-wave radiative forcing: sensitivity study to particle properties and
1001 application to real cases in the region of Barcelona. Atmos. Chem. and Phys., 14(17),
1002 9213-9231.

1003 Sigernes, F., Holmen, S.E., Biles, D., Bjørklund, H., Chen, X., Dyrland, M., Lorentzen,
1004 D.A., Baddeley, L., Trondsen, T., Brändström, U., Trondsen, E., Lybekk, B., Moen, J.,
1005 Chernouss, S., Deehr, C. S. (2014): Auroral all-sky camera calibration. Geosci. Instrum.
1006 Method. Data Syst., 3, 241–245, 2014. doi:10.5194/gi-3-241-2014.

1007 Stier, P., Seinfeld, J. H., Kinne, S., Boucher, O. (2007): Aerosol absorption and radiative
1008 forcing. Atmos. Chem. Phys., 7(19), 5237-5261.

1009 Stone, R.S., Herber, A., Vitale, V., Mazzola, M., Lupi, A., Schnell, R.C., Dutton, E.G.,
1010 Liu, P.S.K, Li, S.-M., Dethloff, K., Lampert, A., Ritter, C., Stock, M., Neuber, R.,
1011 Maturilli, M. (2010): A three-dimensional characterization of Arctic aerosols from
1012 airborne Sun photometer observations: PAM-ARCMIP, April 2009. J. Geophys. Res.,
1013 115, D13203, doi:10.1029/2009JD013605.

1014 Mullikin, J.C., van Vliet, L.J., Netten, H., Boddeke, F.R., Van der Feltz, G., Young, I.T.
1015 (1994): Methods for CCD camera characterization. IS&T/SPIE 1994 International
1016 Symposium on Electronic Imaging: Science and Technology, 73-84. Stumpfel, J., Tchou,
1017 C., Jones, A., Hawkins, T., Wenger, A., Debevec, P. (2004): Direct HDR capture of the
1018 sun and sky. In Proceedings of the 3rd international conference on Computer graphics,
1019 virtual reality, visualisation and interaction in Africa (pp. 145-149). ACM.

Tohsing, K., Schrempf, M., Riechelmann, S., Schilke, H., Seckmeyer, G. (2013): Measuring high-resolution sky luminance distributions with a CCD camera. Appl. Optics, 52(8), 1564-1573.

Titos G, Foyo-Moreno I, Lyamani H, Querol X, Alastuey A, Alados-Arboledas L. (2012): Optical properties and chemical composition of aerosol particles at an urban location: An estimation of the aerosol mass scattering and absorption efficiencies, J. Geophys. Res., 117, D04206, doi:10.1029/2011JD016671,.

Titos G., Lyamani H., Pandolfi M., Alastuey A., Alados-Arboledas L. (2014): Identification of fine (PM1) and coarse (PM10-1) sources of particulate matter in an urban environment. Atmos. Environ., 89, 593-602.

Tomasi, C., Kokhanovsky, A.A., Lupi, A., Ritter, C., Smirnov, A., O'Neill, N.T., Stone, R.S., Holben, B.N., Nyeki, S., Wehrli, C., Stohl, A., Mazzola, M., Lanconelli, C., Vitale, V., Stebel, K., Aaltonen, V., de Leeuw, G., Rodriguez, E., Herber, A.B., Radionov, V.F., Zielinski, T., Petelski, T., Sakerin, S.M., Kabanov, D.M., Xue, Y. Mei, L., Istomina, L., Wagener, R., McArthur, B., Sobolewski, P.S., Kivi, R., Courcoux, Y., Larouche, P., Broccardo, S., Piketh, S.J., Stohl, A. (2015): Aerosol remote sensing in polar regions. Earth-Sci. Rev., 140, 108-157.

Torres, B., Dubovik, O., Fuertes, D., Lapyonok, T., Toledano, C., Schuster, G. L., Goloub, P., Blarel, L., Barreto, A., Mallet, M., Tanré, D. (2016): Advanced characterization of aerosol properties from measurements of spectral optical depth using the GRASP algorithm. Atmos. Meas. Tech. Discuss., doi:10.5194/amt-2016-334.

Urquhart, B., Kurtz, B., Dahlin, E., Ghonima, M., Shields, J. E., Kleissl, J. (2014): Development of a sky imaging system for short-term solar power forecasting. Atmos. Meas. Tech., 8, 875–890, 2015.

Voss, K.J., Zibordi, G. (1989): Radiometric and geometric calibration of a visible spectral electro-optic "fisheye" camera radiance distribution system. J. Atmos. Ocean. Tech., 6, 652–662.

Widenhorn, R., Blouke, M.M., Weber, A., Rest, A., Bodegom, E. (2002): Temperature dependence of dark current in a CCD. Proc. SPIE, 4669, 193-201.Wild, M. (2012): Enlightening global dimming and brightening. Bull. Amer. Meteor. Soc., 93, 27–37.

1056

1057

1058

1059

1060

1061

1062

1063

1064

1065

1066

1067

1068

1069

1070

1071

1072

1073

1074

1075

1076 **List of Figure Captions**

1077 Figure 1: Spectral responses of the three channels (blue, green and red) of the CCD (panel a), of
1078 the infrared (IR) cut-off filter (panel b), and of the three channels of the camera (CCD plus infrared
1079 cut-off filter; panel c). The effective wavelengths of the camera for lunar applications are marked
1080 in panel c.

1081 Figure 2: Zenith (panels a and b), Azimuth (panels c and d) and FOV (panels e and f) viewed by
1082 each camera pixel at Granada (panels a, c and e) and Valladolid (panels b, d and f). Azimuth is
1083 defined from 0º (North) to 360º being East 90º and West 270º.

1084 Figure 3: Sensitivity of the camera pixels for each channel as a function of pixel counts for both
1085 Granada (panel a) and Valladolid (panel b) cameras. The shadow band around the lines represents
1086 the standard deviation.

1087　Figure 4: Dark frames obtained with the Granada camera for different temperatures (T) and
1088　exposure times (ET). The signal shown is multiplied by 4 in order to be better appreciated.

1089　Figure 5: Most frequent value in a dark frame as a function of temperature (T) and logarithm of
1090　the exposure time (ET), for the three Granada camera channels.

1091　Figure 6: Non-HDR (upper; panels a, b and c) tone mapped sky images before removing
1092　background signal (middle; panels d, e and f) and tone mapped sky images with background
1093　corrected (bottom; panels g, h and i). Images corresponds to Granada 21st July 2016, 00:40UTC
1094　(left; panels a, d and g); Granada 20th May 2015, 21:25UTC (middle; panels b, e and h); Valladolid
1095　3rd August 2015, 02:40UTC (right; panels c, f and i). The non-HDR image at Valladolid was taken
1096　under colorless conditions. Pixels with zenith angle above 80º are masked except for non-HDR
1097　images.

1098　Figure 7: Determination coefficient (r^2) between the background pixel signal and the AOD
1099　assumed at each channel. These values are shown for each channel at Granada (left) and
1100　Valladolid (right). Pixels with zenith angle above 80º are masked.

1101　Figure 8: Averaged background HDR images obtained at Granada (panel a) and Valladolid (panel
1102　b). Images are not tone mapped and pixels with zenith angle above 80º are masked.

1103　Figure 9: Normalized lunar almucantar radiances from camera (panel a) and simulated ones by
1104　GRASP (panel b) for Granada 21st July 2016, 00:40UTC. Panel c shows the ratio of normalized
1105　camera radiance to normalized GRASP radiance along the night 20th-21st May 2016 as a function
1106　of azimuth.

1107　Figure 10: Normalized radiance from camera as a function of simulated by GRASP for 8 different
1108　nights at 469 nm (panel a), 533 nm (panel b) and 608 nm (panel c).

1109　Figure 11: Box plots for the relative distribution of ΔNR at 469 nm (panel a), 533 nm (panel b)
1110　and 608 nm (panel c) for different azimuth intervals. The box limits are the 25 and 75 percentiles,
1111　the error bar is the standard deviation, the circle is the mean, the red line inside the box is the
1112　median, the crosses are the 5 and 95 percentiles, and the triangles are the 1 and 99 percentiles.

1113　Figure 12: Box plots for the relative distribution of ΔNR at 469 nm (panel a), 533 nm (panel b)
1114　and 608 nm (panel c) for different MZA intervals. The box limits are the 25 and 75 percentiles,
1115　the error bar is the standard deviation, the circle is the mean, the red line inside the box is the
1116　median, the crosses are the 5 and 95 percentiles, and the triangles are the 1 and 99 percentiles.

1117　Figure 13: Spectral AOD (panel a) and Angström Exponent (panel b) at day and night from 2nd to
1118　3rd August 2015 at Valladolid. Crosses and points represent nocturnal and diurnal data,
1119　respectively.

1120　Figure 14: Evolution of the real (panel a) and imaginary (panel b) refractive indices, sphere
1121　fraction (panel c) and SSA (panel d) at Valladolid from 2nd to 3rd August 2015. Diurnal values
1122　retrieved by AERONET are represented as circles, while nocturnal values retrieved by GRASP,
1123　using normalized camera radiances and nocturnal AOD, are represented by crosses with their
1124　error bars.

1125　Figure 15: Parameters of the fine (panels a, c and e) and coarse (panels b, d and f) aerosol size
1126　distributions from AERONET (black circles) and from GRASP retrieval using normalized camera

1127   radiances and nocturnal AOD (blue crosses with error bars) at Valladolid from 2nd to 3rd August
1128   2015.